Revised submission to *ACS Applied Nano Materials*, September 2018

# Photocatalytic Carbon Nitride Materials with Nanoscale Features Synthesized from the Rapid and Low-Temperature Decomposition of Trichloromelamine

**Anthony T. Montoya and Edward G. Gillan***

Department of Chemistry, University of Iowa, Iowa City, Iowa 52242

Email: edward-gillan@uiowa.edu ORCID (Edward Gillan): 0000-0002-2047-0929

**Abstract**

Polymeric carbon nitride ($C_3N_4$) materials have attracted broad interest in many photocatalytic reactions. This work describes the structural and photocatalytic properties of carbon nitrides from the rapid exothermic decomposition of a trichloromelamine (TCM) precursor at temperatures as low as 180 °C. The use of different reaction conditions produced orange-colored aggregates with nanoplate or sheet-like morphologies. The carbon nitride compositions and physical properties are comparable to carbon nitrides grown from commonly used melamine (MA) and dicyandiamide (DCDA) precursors. Elemental analysis yields compositions fitting $C_3N_{4+x}H_y$ ($0.2<x<0.6$ and $1.8<y<1.9$) and XRD, IR, NMR, and XPS analysis are consistent with cross-linked polymeric heptazine ($C_6N_7$) based carbon nitride network structures with bulk compositions near $C_3N_4$. The darker product color is consistent with smaller band gaps for TCM derived polymeric carbon nitrides compared to MA or DCDA derived analogs (~2.4 vs. 2.6 eV). A comparison of carbon nitrides was made for the oxidative photocatalytic degradation of methyl orange dye under both UV and filtered visible light illumination. TCM derived carbon nitride is capable of degrading over 70% of the dye in two hours of UV illumination and ~50% in 2.5 hours of visible light illumination. UV photocatalytic hydrogen evolution reactions were also performed after photodeposition of Pt, Pd, or Ag nanoparticle co-catalysts onto the carbon nitride surface. Quantitative elemental analysis Combining the Eg and VB results leads to approximate simplified ean ideal 1 wt% solution concentrations. The photocatalytic production of hydrogen using several carbon nitrides was monitored and quantified in real-time using portable mass spectrometry. TCM derived carbon nitride with a Pt co-catalyst achieved hydrogen evolution rates as high as 260 μmol $h^{-1}$ $g^{-1}$. The amount of photodeposited metal, carbon nitride surface area, and the network's structural ordering all appear to impact UV photocatalytic $H_2$ evolution production.

**Keywords:** carbon nitride, trichloromelamine, exothermic, semiconductor, photocatalysis, water splitting, dye oxidation

## Introduction

Nitrogen-rich polymeric carbon nitride materials have received sustained interest as a metal-free photocatalyst and catalyst support.[1-9] This extensive interest is despite the fact that the photocatalytic properties are often modest versus crystalline inorganic oxide photocatalysts and there are often substantial variations in materials made from different synthetic preparations. These variations are sometimes less evident because this diverse family of polymeric carbon nitrides are frequently referred to as graphitic $sp^2$ hybridized structures (g-$C_3N_4$) with formulas analogous to $sp^3$ hybridized $Si_3N_4$ or fully condensed C-N graphite layers existing as an ordered line phase. In truth, most visibly colored semiconducting "g-$C_3N_4$" materials from thermal processing of molecular precursors consist of crosslinked heptazine ($C_6N_7$) units in a polymeric network structure with significant residual hydrogen in $NH_x$ bonds (generally $C_3N_{4+x}H_y$). Variations in local composition, structural ordering and condensation, enhancement or disruption in π bonding structures and local planarity, can all potentially influence optical absorption properties and effectiveness of charge carrier use in photocatalytic reactions. While the g-$C_3N_4$ term is very commonly used for these semiconducting π conjugated C-N polymers, other terms such as PCN (polymeric carbon nitrides), GCN (graphite-like carbon nitride) and gCN(H) or pCN(H) have been recently recommended or used.[10-12] Conjugated nitrogen-rich carbon-nitride networks are typically formed through the moderate temperature (~500 °C) thermal condensation and ring expansion of nitrogen containing precursors, with cyanamide (NC-$NH_2$) being the one of the simplest precursors.[3, 13-14] Likely as a consequence of having N-H bonds in the precursor, these nitrogen-rich carbon nitrides often contain hydrogen.[15-16] Two precursors commonly used for bulk $C_3N_4$ growth are dicyandiamide (DCDA, $C_2H_4N_4$) and melamine (triaminotriazine, $C_3N_3(NH_2)_3$).[17-19] The generally accepted local structure of $sp^2$ hybridized carbon nitride materials resulting from these precursors is that they are composed of linked tri-s-triazine (heptazine, $C_6N_7$) units. These structurally disordered carbon nitride materials have a $C_xN_yH_z$ composition and are akin to condensed and crosslinked polymers (melon) and early macromolecular heptazine polymers as $C_3N_4$ intermediates.[20-22] The heptazine structural model is supported by X-ray and neutron diffraction, IR, NMR, and XPS analysis.[15, 23-27] The high temperature synthesis conditions lead to the volatilization of small C-N containing compounds, leading to the variations in bonding and stoichiometric proximity to a $C_3N_4$ composition.[10] We previously showed that carbon nitrides near $C_3N_4$ compositions grown from triazine-based precursors have a heptazine rather than a triazine extended structure. The direct evidence for this is that only potassium cyamelurate ($K_3C_6N_7O_3$) is produced during carbon nitride chemical degradation in refluxing 3M KOH and this heptazine oxyanion has strong luminescent properties in line with other molecular heptazines.[15, 28] Under similar caustic base reactions, triazines such as melamine do not condense into larger heptazine structures. There are several studies, both early and recent, that have designed novel precursors or network formation strategies to produce

films and bulk materials with strong graphitic (condensed) $C_3N_4$-like products or triazines connected by imide links (polytriazine imides – PTI). In one case, a single-source triazine precursor with trimethylsilylamine and halide terminal groups was used in inert chemical vapor deposition (CVD) at 500 °C. The film products showed little or no hydrogen, likely due to absence of direct N-H bonds in the precursor and compositions and properties consistent with a graphitic $C_3N_4$.[29] The synthesis of PTI structures and more condensed graphite-like triazine analogs has also been successful using novel mixed alkali halide salt flux reaction environments.[30] As noted in a recent extensive in-depth review of carbon nitride structure and property analysis and interpretation, some analytical techniques cannot clearly distinguish heptazine from triazine-based extended structures.[10]

Despite a clear variation in composition, structure, and resulting properties, polymeric carbon nitride materials have found extensive use in photocatalytic oxidation and reduction reactions, including environmental applications such as the oxidative degradation of model aqueous organic pollutants[2, 31-32] or gas phase photolysis of NO.[33] Applications in organic reactions include use as a photoinitiator in radical polymerization[34] and selective oxidation of alcohol or sulfonate functional groups.[35-36] The photocatalytic production of hydrogen from aqueous systems has been demonstrated with carbon nitrides decorated with Pt co-catalysts.[4, 37-39] Polymeric $C_3N_4$ structures have also been incorporated into electrode designs for photoelectrochemical hydrogen evolution reactions (HER).[6, 40] Silica templates have been utilized to generate mesoporous polymeric $C_3N_4$ products with higher surface area that leads to greater photocatalytic activity.[41-42] Thermal or chemical exfoliation of bulk carbon nitrides produces colloidal nanoflakes that lead to improved photocatalytic activity.[43-44] The level of structural order in the π-stacking direction is often on the order of a few nanometers and can vary with different synthetic methods. The use of co-monomers to add other functional groups or form heterojunctions between differently structured carbon nitrides has been shown to enhance catalysis.[33, 45-46] Composites and heterojunctions between carbon nitrides and other conducting or semiconducting materials have also been studied to improve light absorption and charge separation properties.[2, 9, 47-50] Such nanoscale and macroscale changes can influence physical properties of the carbon nitrides. Given the typical structural disorder associated with these polymer-like structures, recent work has identified and exploited important carbon nitride defects to enhance its catalytic properties.[51-53]

The work detailed here describes the structure and photocatalytic behavior of polymeric carbon nitrides produced from the rapid and exothermic self-decomposition of a thermochemically unstable trichloromelamine (TCM, $(C_3N_3(NHCl)_3)$ and directly compares its properties with carbon nitride materials produced from melamine and DCDA precursors. Our previous work established the

thermochemically reactive nature of the TCM precursor under external heating (<250 °C) or in contact with a resistively heated filament.[15, 26] TCM-derived polymeric carbon nitrides are very stable in organic solvents, acids and bases. Though TCM has the advantage of a low reaction temperature, higher synthesis temperatures and post-reaction annealing were explored to compare their effect on photocatalytic activity. The rapid combustion-like decomposition and condensation of TCM leads to carbon nitrides that form as large nanoscale to small micrometer-sized plate-like particles made up of smaller fused regions. The TCM-derived polymeric carbon nitride materials were examined as photocatalysts in the oxidative degradation of methyl orange dye under UV and filtered visible light compared to carbon nitrides from DCDA and melamine. Solution photoreduction reactions added Pt, Pd, or Ag nanoparticle co-catalysts onto the carbon nitride surface for HER. HER reductive photocatalysis was successfully performed in aqueous solution using triethanolamine as a sacrificial oxidant, and hydrogen gas evolution was conveniently measured in real-time using a portable mass spectrometer.

**Experimental Procedures**

Trichloromelamine ($C_3N_3(NHCl)_3$, TCM, GFS Chemical 98%) was stored in an argon atmosphere glovebox. Melamine ($C_3H_6N_6$, MA, Aldrich 99+%) and dicyandiamide ($C_2H_4N_4$, DCDA, Alfa Aesar, 99%), methanol (ACS certified, Fisher), triethanolamine (Alfa Aesar, 98+%) and methyl orange (85% dye content, Sigma Aldrich) were used as received. Deionized water (18 MΩ) was obtained from a Photronix MiniQuad system.

**Safety warning**: Most carbon nitride formation reactions involve condensation of C-N bonded precursors that can liberate hazardous byproduct gases. For the TCM exothermic decomposition described here, evolved gases include HCN, $Cl_2$, HCl and other cyanogen based products. Careful hood ventilation must be utilized and pressure calculations performed on closed systems that can rapidly increase in pressure during synthesis. Also appropriate hood shields and PPE must be employed during synthesis and product workup and isolation.

**Carbon nitride syntheses**. Inside an argon atmosphere glovebox, TCM (5.0 g, 21.8 mmol) was loaded into a glass lined stainless steel reactor (Parr Instruments, 125 mL, model 4752). The reactor was sealed and removed from the glovebox. The reactor was put into a fitted Glas-Col heating mantle and heated to 250 °C at 10 °C/min. The external temperature, internal temperature, and internal pressure were recorded as the system was heated. Near 220 °C there was a spike in internal temperature (from ~120 °C to 250 °C) and pressure (1000 psi), at this point, the heating mantle was turned off. As the system cooled the pressure equilibrated to 350 psi. The reactor was slowly vented into the fume hood and then

disassembled. Approximately 1 g of a bright orange sponge-like solid was collected from the inside of the reactor (typically ~20% mass yield). This Parr synthesized product from TCM is referred to as TCM-$C_3N_4$(P).

The as-synthesized TCM-$C_3N_4$(P) was treated at higher temperatures to further anneal the structure. Typically, 100-300 mg of product was loaded into an alumina boat, which was put inside a Pyrex tube closed on one end. The tube was connected to a Schlenk line, evacuated, and back-filled with argon. The tube was put into a clamshell furnace and heated to 500 °C at a rate of 10 °C/min and held for 1 hour. Following annealing, 60-90% of the starting mass was recovered from the boat and a film of white transport was observed at the cool end of the tube. This annealed Parr synthesized product from TCM will be referred to as TCM-$C_3N_4$(P/A).

A single-step high-temperature synthesis method that is typically employed for less reactive precursors was used with the TCM precursor as well with DCDA and melamine (MA) as reference materials. Typically, 400 mg of the carbon nitride precursor was loaded into a Schlenk tube with a test tube insert. An oil bubbler was connected to the side arm for pressure venting and degassed with nitrogen. The tube was clamped in position above a vertically oriented furnace, set to heat to 500 °C at a rate of 10 °C/min and held for 1 hour. The product was collected from the tube insert after cooling and venting the reaction tube. These products from tube heating of TCM, DCDA, and MA will be referred to as TCM-$C_3N_4$(T) (~20% mass yield), DCDA-$C_3N_4$(T) (~45% mass yield), MA-$C_3N_4$(T) (~34% mass yield), respectively.

In order to examine the effect of macroscopic surface area changes on carbon nitride properties, selected products were ball milled in a high-energy ball mill (FormTech FTS 1000). 100 mg of solid was added into a 5 mL stainless steel milling jar with 2x 5 mm steel balls. Milling was performed at 1200 rpm for duration of 5 minutes.

**Carbon nitride characterization**. FT-IR spectra were collected on a Nicolet Nexus 670. Solid samples were prepared as KBr pellets for data collection. Gas samples were analyzed by transferring 5 mL of gas from the reaction vessel into a 10 cm long gas IR cell with KBr windows. Carbon cross polarization magic angle spinning (CP-MAS) solid state NMR experiments were conducted on a Bruker AV III instrument (Bruker Biospin, Billerica, MA) operating at a proton frequency of 500.01 MHz. Solid samples (~70 mg) were spun at 13 KHz in a 4 mm $ZrO_2$ rotor. The contact time was 2 milliseconds and was ramped on the proton channel from 50 to 100%.[54-55] The relaxation delay was maintained at 8 seconds. Proton decoupling was applied using a TPPM sequence with a 3.75 microsecond pulse (66.7

KHz nominal band width). The spectral sweep width was 300 ppm centered at 100 ppm. 1024 data points were acquired and zero filled to 8192 prior to apodization with 100 Hz line broadening. Typically 4096 free induction decays were co-added, to increase S/N 3 spectra were added after transformation. The spectra were referenced indirectly to TMS using 3-methylglutaric acid.[56] Bulk elemental analysis was collected on a Perkin Elmer 2400 Series II CHNS/O analyzer, with 1-2 mg of sample in crimped tin capsules. Powder X-ray diffraction (XRD) was collected on a Bruker D8 DaVinci system (source Cu Kα, 5-80°, 0.050 °/step) with samples deposited on glass slides. Crystallite size estimates were performed using Scherrer analysis. Thermogravimetric-differential thermal analysis (TG-DTA) was performed on a Seiko Exstar 6300 TGA-DTA. Samples were heated up to 1000 °C at a rate of 10 °C/min under air or argon flow. Scanning electron microscopy images were collected on a Hitachi S-4800 FE-SEM. X-ray photoelectron spectra (XPS) for samples pressed on indium foil were collected on a Kratos Axis Ultra DLD XPS. Diffuse reflectance spectra were collected on a Cary 5000 Series UV-Vis-NIR Spectrophotometer (300-800 nm, 10 nm/s). All samples were ball-milled to ensure fine powders that were loaded into the sample cell. Kubelka-Munk conversions were calculated from the software and Tauc plots were generated using $[F(R)hv]^{1/2}$ conversion for indirect band gap calculations. Band gap values were approximated by extrapolating the linear portion of the main absorption edge. Room-temperature photoluminescence measurements were performed using an Agilent Cary Eclipse fluorescence spectrometer (10 nm/s scan rate, auto filters, 5 nm slits) on carbon nitride powders embedded on 1 cm filter paper strips mounted inside a cuvette holder such that the excitation was about 30 degrees from normal of the sample. BET surface area measurements were taken on a Quantachrome NOVA 1200 using approximately 150 mg of solid sample. ICP-OES data was collected on a Varian 720-ES. Samples were dissolved in a heated mixture of 5 mL concentrated $H_2SO_4$ and 1 mL of concentrated $HNO_3$ and diluted in 25 mL volumetric flasks with 5% $HNO_3$.

**Dye photooxidation studies**. The oxidative degradation of methyl orange dye ($C_{14}H_{14}N_3SO_3Na$) was studied using the different ball milled polymeric carbon nitride photocatalysts. A stock 1.0 mM dye solution was first prepared dissolving the solid dye in 18 MΩ water. The stock solution was diluted to 40 μM and adjusted to pH 3 to fit the peak at $\lambda_{max}$ in the range ($\lambda_{MO}$=504 nm, A<2.0) of the UV-vis spectrophotometer (Agilent 8453). To 30 mL beakers, 10 mL of dye solution and 10 mg of carbon nitride catalyst was added. An additional beaker containing only dye was used as to evaluate photo-degradation in the absence of catalyst. Samples were stirred a minimum of 30 minutes to allow dye absorption equilibrium to be reached (dark adsorption). Samples were exposed to UV light (Ace-Hanovia, 450 W Hg lamp positioned 20 cm from the beakers, ~2.6 x $10^{16}$ photons $s^{-1}$ $cm^{-2}$, ~12 $cm^2$ beaker exposure area) in 15-30 minute intervals. The beakers were open to air that provided oxygen for the catalyzed

photooxidation of the dye. After each illumination period, the catalysts were separated from the dye solution by centrifugation (3000 rpm) and the UV-vis spectrum of each solution was collected to quantify the remaining concentration of dye. Experiments were typically carried out for 2 hours of total UV irradiation. For visible light experiments 400 nm long pass filters (Edmund Optics) were used and irradiation times were extended to 2.5 hrs in order to achieve > 20% dye degradation.

**Photocatalytic hydrogen evolution**. For photocatalytic hydrogen evolution tests, the polymeric carbon nitride powders were modified with Pt, Pd, or Ag co-catalysts. Metals were photoreduced onto the powder surface under UV light using $H_2PtCl_6$, $K_2PdCl_6$, or $AgNO_3$ as the metal source. The carbon nitride powder was suspended in a 50% aqueous methanol solution containing an amount of the metal targeting 1 wt% of reduced metal on $C_3N_4$ and using methanol as a sacrificial oxidant. The solution was degassed with argon and exposed to UV light for 2 hours. The solid was collected by centrifugation, rinsed with methanol, and dried in air. In the hydrogen evolution reactions 10 mg of the carbon nitride catalyst (with or without a metal co-catalyst) was dispersed in a 10 mL solution of 10% aqueous triethanolamine ($C_6H_{15}NO_3$, sacrificial oxidant) in a 50 mL Schlenk flask. The solution was degassed with argon and connected to a residual gas analysis mass spectrometer (RGA-MS, Stanford Research Systems QMS 300 series) by capillary to the side arm. Data was collected as a pressure versus time scan, monitoring the masses for nitrogen, argon, hydrogen, water, oxygen, and carbon dioxide. The reactor was exposed to UV light in one-hour intervals and was vented with an argon purge between each UV run in order to return hydrogen concentrations to baseline levels. The molar amounts of hydrogen produced were determined using a pressure signal calibration based on known concentration mixtures of $H_2$/Ar. Details are in our previous report on 3d metal surface-modified titanias for photocatalytic hydrogen evolution using real-time $H_2$ analysis with this RGA-MS system.[57] Quantum yield calculations were based off a 5.2 x $10^{17}$ photons $s^{-1}$ flux for sum of all wavelengths in the Hg emission spectrum at or below 435 nm, additional details can be found in our previous work.[57]

**Results and Discussion**

**Synthesis of polymeric carbon nitride materials from TCM and other precursors**. The thermal decomposition of trichloromelamine (TCM) inside the high-pressure Parr reactor allowed the internal temperature and pressure to be monitored. As the heating mantle reached 250 °C, the interior temperature reached 105 °C immediately before the reaction occurred. The internal walls of the reactor were likely at an intermediate temperature of ~180 °C. As TCM rapidly decomposed, the internal temperature jumped to 230 °C, but quickly cooled back to 150 °C within a minute indicating a sudden brief exothermic decomposition. This temperature change also paired with a pressure increase to 1000 psi at the instant of

decomposition, but dropped to 450 psi after the initial shock. Once the reactor had cooled back to room temperature, the internal pressure had equilibrated to 350 psi. Gas phase IR (**Figure S1**) and mass spectrometry[15] data confirmed the presence of the gas by-products from the TCM decomposition reaction shown in **Scheme 1**. For the Parr reaction where 22 mmol of TCM was used, ~100 mmol of gaseous products were generated based on the final pressure of the reactor. This mmol estimate is consistent with the expected moles of gaseous C/N/H/Cl containing byproducts shown in **Scheme 1**. A visibly porous mass of dark orange carbon nitride solid material was also isolated from this thermally initiated self-propagating decomposition of TCM [TCM-$C_3N_4$(P)].

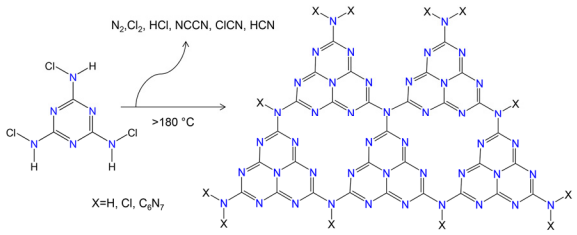


**Scheme 1**. Decomposition of TCM to an ideal ordered polymeric carbon nitride network structure of condensed heptazines. Note that an ideal $C_3N_4$ composition occurs when X = $C_6N_7$.

TG-DTA analysis of the TCM precursor under an argon flow supports the observations from the decomposition reaction, showing the first major mass loss paired with an exothermic event near 180 °C (**Figure S2A**), consistent with our prior work.[26] Rapid mass loss continues for the next 20-30 °C as the stable carbon nitride product forms and condenses. Compared to other precursors, TCM has a lower reaction temperature of carbon nitride product formation. Mass loss is gradual at higher temperatures due to the slow volatilization of $C_xN_yH_z$ fragments from the solid, until complete decomposition by 700 °C. The thermal behavior of TCM helped inform conditions for annealing experiments using the TCM-$C_3N_4$(P) product. Since this Parr reaction product is relatively stable to 500 °C under inert or air atmosphere (**Figure S2B**), this is a suitable temperature to potentially further condense the extended carbon nitride structure. Some mass loss (~ 27%) occurred during inert annealing of TCM-$C_3N_4$(P) at 500 °C and a white film transport grew on the cool end of the annealing tube that was identified by XRD and IR as $NH_4Cl$. This byproduct could result from bound HCl on $NH_2$ terminal groups of the carbon nitride structure that are released upon heating. This annealed Parr product [TCM-$C_3N_4$(P/A)] exhibited a slight darkening relative to the initial orange product.

The TCM precursor exhibits similar product decomposition properties when subjected to synthesis conditions typically used for more stable carbon nitride precursors such as melamine and DCDA (*i.e.*,

heating to 500 °C in a $N_2$ flushed tube reactor). Note that some carbon nitride syntheses are reportedly take place in open reactors exposed to air. In order to limit potential oxygen contamination of the carbon nitride products, inert nitrogen gas blankets were used for all heated tube reactions in this work. In the tube reactor, the visible changes are observed during TCM decomposition. Near 180 °C, gas evolution occurs from the TCM precursor as shown by an increased gas exit rate at the oil bubbler and a light yellow solid transport appearing at the top of the tube reactor outside the furnace, later identified as $NH_4Cl$ by XRD. The more stable and slowly condensing DCDA and melamine precursors did not show similar rapid gas evolution reactions when subjected to the same 500 °C inert tube reactions. The TCM, DCDA, and melamine products from inert tube (T) heating are TCM-$C_3N_4$(T), DCDA-$C_3N_4$(T), and MA-$C_3N_4$(T), respectively. The TCM-$C_3N_4$(P) and TCM-$C_3N_4$(T) products have a similar mass yield of about 20% while DCDA-$C_3N_4$(T) and MA-$C_3N_4$(T) are higher at 45% and 35% respectively. This is due to a greater mass loss from the heavier chlorine atoms present in the TCM precursor. A visual comparison of polymeric carbon nitride materials produced in this study is shown in **Figure 1**. As shown in **Figure 1a**, the TCM carbon nitride product forms as porous sponge-like fused mass, suggesting some possible melt/gas evolution process. Upon grinding, all powders are similarly coarse powders with the TCM products having more significant visible absorption and orange color versus the lighter yellow carbon nitride powders from MA and DCDA.

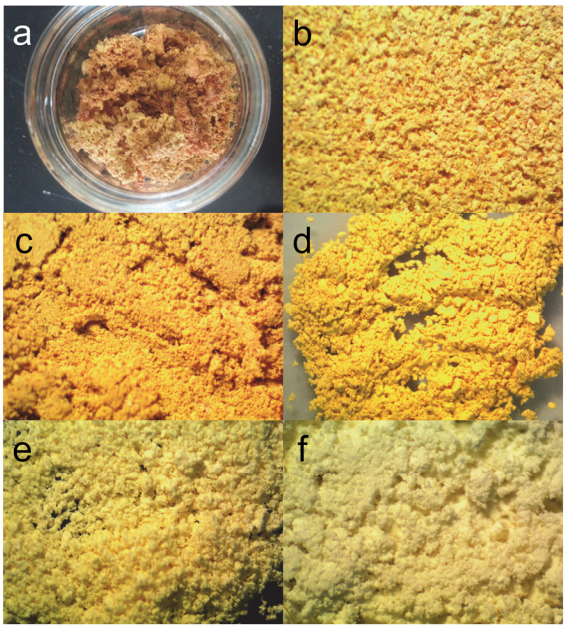


**Figure 1.** Photos of (a,b) TCM-$C_3N_4$(P), (c) TCM-$C_3N_4$(P/A), (d) TCM-$C_3N_4$(T), (e) MA-$C_3N_4$(T), and (f) DCDA-$C_3N_4$(T) powders.

**Chemical and structural characterization of polymeric carbon nitride materials.** Since carbon nitrides are generally extended and intractable structures akin to crosslinked polymers, bulk chemical analysis is an important component for clear composition comparisons and consistent structural analysis interpretations. CHN combustion analysis yields the composition data on TCM and comparative DCDA and melamine $C_3N_4$ products shown in **Table 1**. All products are more nitrogen-rich than the general formula of $C_3N_4$, instead fitting $C_3N_{4+x}H_y$ ($0.2<x<0.6$, $1.8<y<1.9$) consistent with both our previous TCM-$C_3N_4$ products and $C_3N_4$ prepared from other precursors.[15, 26, 43-44, 58] Prior chemical analysis on TCM-$C_3N_4$(P) shows that bulk chlorine residues are very small (e.g., $C_3N_{4.51}H_{1.6}Cl_{0.02}O_{0.12}$).[26] Air or moisture sensitive dangling bonds from precursor decomposition reactions can lead to important variations on composition, particularly hydrogen content. As an extreme example, a hydrogen-free triazine azide precursor [$(C_3N_3(N_3)_3$] yielded a bulk H-free ~$C_3N_{4.6}$ product that slowly reacts in air to form a hydrogen containing air-stable product.[59] Analysis of the C:N:H ratios in carbon nitrides have been described as a possible indicator for degree of condensation in these heptazine (or triazine)-based polymeric carbon nitrides.[10] The products here all show compositions near $C_3N_4$ but also all contain hydrogen, some likely bound as $NH_2$ terminal sites in the structure. The presence of hydrogen may also cause of a disruption of in-plane ordering or conjugation in the long range structure through formation of >NH bridges between heptazine units. In considering the case of bridging NH units connecting heptazines, a bulk formula of $C_3N_{4.5}H_2$ (or $C_6N_9H_4$) could be formulated as $(C_6N_7)(NH_2)(NH)_2$ with a terminal $NH_2$ unit and two bridging NH unit for each core heptazine, consistent with recent analysis of extensive carbon nitride literature and analysis.[10] Higher temperature TCM decomposition and annealing lead to potentially more condensed polymeric carbon nitride products with a higher total CHN content (Table 1). Volatile components eliminated during heating may contain other elements such as O or Cl, such as observed $NH_4Cl$ during TCM-$C_3N_4$(P) annealing. The remaining mass may be oxygen from surface oxidation or adsorbed water, which would also increase the observed H content.[10]

**Table 1**. CHN elemental analysis of $C_3N_4$ products

| Product (Method) | C wt% | N wt% | H wt% | Total wt % CNH | Formula |
|---|---|---|---|---|---|
| **TCM-$C_3N_4$(P)** | 33.12 | 54.06 | 1.69 | 88.87 | $C_3N_{4.2}H_{1.8}$ |
| **TCM-$C_3N_4$(P/A)** | 34.27 | 61.89 | 1.76 | 97.92 | $C_3N_{4.6}H_{1.8}$ |
| **TCM-$C_3N_4$(T)** | 34.41 | 58.65 | 1.84 | 94.90 | $C_3N_{4.4}H_{1.9}$ |
| **MA-$C_3N_4$(T)** | 33.85 | 60.61 | 2.16 | 96.62 | $C_3N_{4.6}H_{2.2}$ |
| **DCDA-$C_3N_4$(T)** | 34.03 | 60.02 | 2.41 | 96.46 | $C_3N_{4.5}H_{2.5}$ |

The IR spectra of the polymeric carbon nitride products (**Figure 2**) show significant similarities between the different decomposition methods and precursors used. The broad band near 3200 $cm^{-1}$ corresponds to N-H stretches for $NH_x$ bridging or terminal groups in the polymeric $C_3N_4$ structure. The bands from 1200-1700 $cm^{-1}$ correspond to C-N (1200-1480 $cm^{-1}$) and C=N (1570-1640 $cm^{-1}$) stretches in the ring structure. The sharp peak near 810 $cm^{-1}$ is usually assigned to the characteristic of the ring breathing mode for conjugated heptazine heterocycles.[8, 39] This band for both triazine and heptazine rings falls near 800 $cm^{-1}$,[44] but in comparison to the corresponding triazine ring stretch for TCM at 796 $cm^{-1}$, the product vibration occurs at higher frequency. The peak shift for triazines to heptazines in consistent with observations from both experiment and theory.[10, 60] Additionally, a small peak near 900 $cm^{-1}$ is observed in heptazine versus triazine extended structures.[10] As noted earlier, heptazine core units were verified as being present in TCM-$C_3N_4$(P) products,[15] and the broader array of IR peaks agree with those observed for polymeric $C_3N_4$ produced from TCM using rapid, low temperature methods as well as those produced from thermal decomposition of melamine or cyanamide.[10, 26, 61-62] As compared to the other carbon nitrides here, the TCM-$C_3N_4$(T) product (Figure 2c) has less well-defined peaks, particularly near 1200 $cm^{-1}$ region, which may indicate some lower structural ordering in TCM-$C_3N_4$(T).

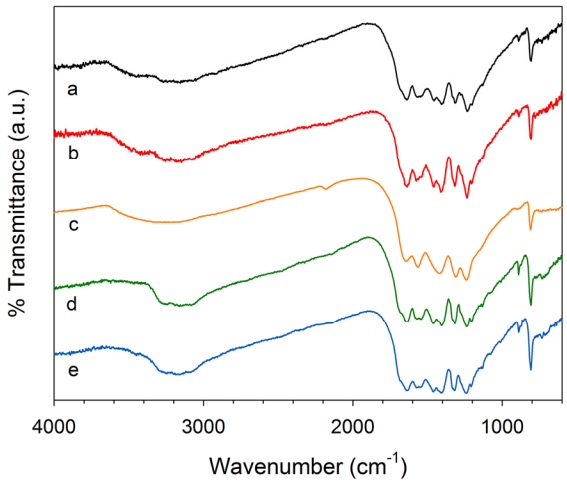


**Figure 2**. IR spectra of (a) TCM-$C_3N_4$(P), (b) TCM-$C_3N_4$(P/A), (c) TCM-$C_3N_4$(T), (d) MA-$C_3N_4$(T), and (e) DCDA-$C_3N_4$(T).

The local carbon structure of the TCM-$C_3N_4$ products was examined by $^{13}C$ CP-MAS NMR which showed two resonances near 156 and 164 ppm (**Figure S3)**. These two signals fit with a heptazine motif present in the polymeric $C_3N_4$ structure, with the peak at higher chemical shift assigned to the exterior heptazine carbon and the lower chemical shift peak assigned to the interior carbon. The position of these peaks matches with our previous observations for $C_3N_4$ produced from TCM as well as from a 2,5,8-

triazido-s-heptazine precursor.[15, 63] The carbon peak shifts also match with those for molecular heptazines.[23, 64] In contrast, the peak shift for carbon in a triazine environment is typically near 168-170 ppm.[23, 26, 58] This provides further support for the formation of heptazine units in polymeric $C_3N_4$ from TCM decomposition. The peak shifts were also in agreement with values reported for polymeric $C_3N_4$ produced from melamine and dicyandiamide described as having a heptazine repeat structure. **Table S1** shows a comparison NMR chemical shift data on several related polymeric carbon nitrides.[10, 22, 52, 58, 65-66] Note that there is some disagreement on the uniqueness of heptazine versus triazine $^{13}C$ NMR peak shifts,[10] though there are likely challenges in producing a purely triazine-based extended structure under thermal precursor processing may yield mixed triazine-heptazine condensation products.

While elemental analysis, IR, and NMR yield bulk analytical information, surface sensitive XPS is a useful complement for surface compositional analysis and information about the local bonding environment around carbon (C 1s) and nitrogen (N 1s) as well O 1s, and Cl 2p regions. **Table S2** summarizes peak fittings and compositional data for TCM-$C_3N_4$ powders examined on indium foil to limit background carbon interference, and the XPS spectra are shown in **Figure S4**. Two peaks are present in the C 1s spectrum near 284.5 eV and 288 eV. The peak at 284.5 eV was typically lower intensity and is consistent with adventitious surface carbon contamination commonly detected in air-exposed XPS samples.[10] While this signal could also indicate some C-C bonding, the high nitrogen content in these polymeric carbon nitrides makes that a less likely assignment as it would necessitate some N-N bonding. The major C1s signal at 288 eV agrees with carbon in an $sp^2$ coordination environment as would be expected of an interior or exterior $sp^2$ carbon in the heptazine subunit of polymeric carbon nitrides (see **Scheme 1**).[24, 26, 39] The N 1s spectrum shows a major peak at 398 eV with a shoulder at higher energy that is deconvoluted into two peaks at 400 eV and 401 eV. The peak at 398 eV can be assigned to the bridging C-N-C on the exterior of the heptazine ring.[10] There are two different three-coordinate nitrogen sites in the ideal layered $C_3N_4$ structure as shown in **Scheme 1**, one in the center of the heptazine ring and the second acting as the N linker between heptazine units. Consistent with the IR and chemical analysis, there should be significant bridging NH and terminal $NH_2$ in these structures. The higher energy ~400 eV shoulder peaks are a reasonable fit to N-$(C)_3$, HN-$(C)_2$, or $(H)_2$N-C along with some surface N-O at higher energies near 404.5 eV.[24, 26, 39]

The bulk elemental analysis data above shows that the $C_3N_4$ materials are mainly C/N/H but XPS also identified the presence of surface O, and in some cases Cl, in TCM-derived carbon nitrides. The surface levels of oxygen and chlorine are slightly higher than our previously reported bulk elemental analysis as noted above.[26] Trace surface chlorine was mainly present in TCM-$C_3N_4$(P) and was smaller or absent

from the TCM-$C_3N_4$(P/A) or TCM-$C_3N_4$(T) products prepared by extended heating at 500 °C. This agrees with the previously described increase of total CHN content and observed $NH_4Cl$ transport in annealed products. The surface oxygen content decreased significantly in the TCM-$C_3N_4$(P/A) product. The surface compositions measured by XPS for the TCM-$C_3N_4$ products fit formulas of $C_3N_{3.6}O_{0.8}Cl_{0.2}$ for TCM-$C_3N_4$(P), $C_3N_{3.4}O_{0.2}$ for TCM-$C_3N_4$(P/A), and $C_3N_{2.6}O_{0.8}Cl_{0.05}$ for TCM-$C_3N_4$(T) (**Table S2)**. These compositions have a lower nitrogen content or higher carbon content than the bulk elemental analysis (~$C_3N_{4+x}$ with $x \geq 0.2$). Since these compositional analysis methods measure different parts of the sample (bulk versus surface), it is not surprising that these values differ. The calculated carbon content on the surface include the adventitious carbon peak at ~284 eV and if it is excluded from the XPS surface composition analysis, then the XPS and CHN data are similar (*e.g.,* for TCM-$C_3N_4$(P/A) becomes $C_3N_{4.2}$ vs. $C_3N_{3.4}$, Table S2).

Powder XRD of various polymeric carbon nitride products shows generally close similarity in their lack of long range order (**Figure S5**). The major peak at 27.5° (d=3.24 Å) is attributed to the spacing between the tri-s-triazine layers or sheets in a polymeric $C_3N_4$ structure. A weaker secondary peak at 13° (d=6.81 Å) is assigned to the in-plane repeat of tri-s-triazine units.[14] The major peak near 27.5° is prominent in all of the polymeric carbon nitrides, though it is consistently broader in TCM-$C_3N_4$(T) products. An estimate of crystallite size or ordering along this interlayer spacing direction from this XRD peak data is 6-8 nm for Parr TCM, DCDA, and melamine products and a much lower ordering near 2 nm for the TCM-$C_3N_4$(T) product (corresponding to ~6 layers). A decrease in the intensity and broader of this characteristic carbon nitride layering peak has been reported in polymeric carbon nitrides annealed above 500 °C.[44] Recent extensive analysis of XRD interlayer stacking in polymeric carbon nitrides highlights how interlayer bending or buckling that is likely present in these structures can lead to XRD peaks near 26° versus an ideal 28°.[10] Hydrogenation and >NH bonds between heptazines could enhance planar structural disorder leading to broad XRD peaks.

The analysis of carbon nitride morphologies by SEM shows that TCM derived polymeric $C_3N_4$ products form large aggregates above 1 μm (**Figure 3**). These appear to have smooth faces, but have fractures along the edges that reveal large nanometer size features. The produced carbon nitride appears to grow in an aggregated mass of irregularly shaped nanoscale to microscale plate or sheet-like structures that likely form as a consequence of rapid combustion-like TCM decomposition. When compared with TCM-$C_3N_4$(P), TCM-$C_3N_4$(P/A) exhibits many of the same features, including ~100-200 nm sized plate-like particles. There are some expansion of pores and perhaps some smoothing of surface features on some particles upon annealing (see **Figure S6A**). The TCM-$C_3N_4$(T) product prepared by direct inert tube

heating at 500 °C shows larger more extended structures on the order of 10-40 μm that contain large pores or depressions on the order of ~500 nm, likely a consequence of rapid gas evolution with precursor condensation to form the carbon nitride. The surfaces of these larger structures contain smooth 1-5 μm fragments with rough edges that are fairly thin (~100 nm, Figure 4 bottom row). Additional SEM images showing different magnifications for the polymeric carbon nitrides are in **Figure S6**. One potential advantage of rapid TCM self-decomposition/condensation is that it may open up additional avenues for nanoscale (~100 nm) polymeric carbon nitride particulate/plate-like growth on heterostructured materials.

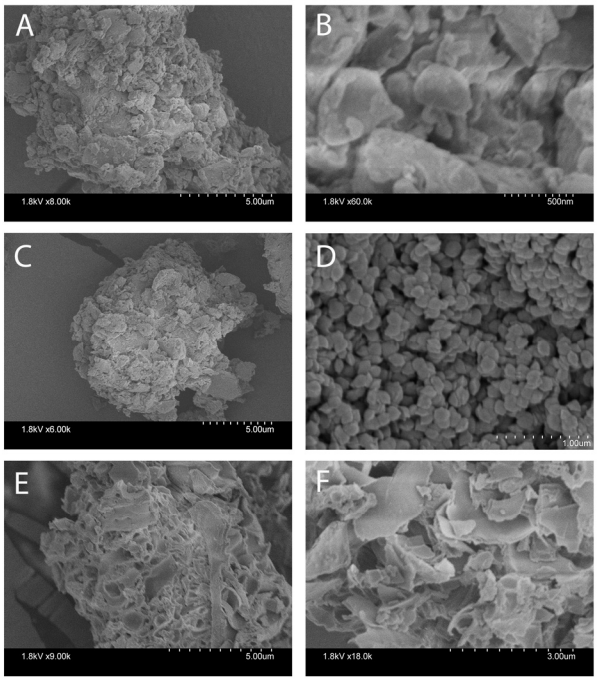


**Figure 3**. SEM images of (A, B) TCM-$C_3N_4$(P), (C, D) TCM-$C_3N_4$(P/A), and (E, F) TCM-$C_3N_4$(T).

While SEM imaging indicates that the TCM derived carbon nitrides show some large scale porosity, BET surface area analysis shows that TCM-$C_3N_4$(P) has a fairly low surface area of 3.3 $m^2$ $g^{-1}$, comparable to our previously reported 5 $m^2$ $g^{-1}$ for a TCM product decomposed via hot wire initiation, and consistent with the packed and aggregated flake-like SEM images.[26] Following ball-milling, the surface area of TCM-$C_3N_4$(P) nearly doubled to 6.2 $m^2$ $g^{-1}$. Higher temperature treatments resulted in a negligible increase to 4.2 $m^2$ $g^{-1}$ for TCM-$C_3N_4$(P/A) and 4.1 $m^2$ $g^{-1}$ for TCM-$C_3N_4$(T). The surface area of TCM-$C_3N_4$(P/A) and TCM-$C_3N_4$(T) increased to 11.4 $m^2$ $g^{-1}$ and 8.3 $m^2$ $g^{-1}$ respectively after ball-milling. The unmilled surface areas of TCM-$C_3N_4$ products are lower than a 7.6 $m^2$ $g^{-1}$ surface area measured for DCDA-$C_3N_4$(T) produced in our experimental setup, which is comparable to reported values.[39] Nitrogen adsorption-desorption isotherms are shown in **Figure S12** and have shapes consistent with Type II or III

isotherms that are observed for non-porous or macroporous solids with relatively weak absorption.[67] The estimated pore diameters are 95 Å, 44 Å, and 69 Å for TCM-$C_3N_4$(P), TCM-$C_3N_4$(P/A), TCM-$C_3N_4$(T), respectively and indicate significant pore reduction on annealing the rapidly formed Parr product at 500 °C. This is consistent with a view of carbon nitrides as flexible polymeric structures. Some carbon nitride preparations that targeted materials with nanoflake geometries report mesoporous Type IV isotherm behavior while others report Type III isotherms for melamine-derived macroscale materials.[24, 33, 41-42, 49]

Diffuse reflectance UV-vis spectroscopy was used to examine the optical absorption properties and band gaps of the orange colored TCM carbon nitrides as compared to their lighter yellow MA and DCDA analogs. The reflectance data was converted to absorbance using the Kubelka-Munk function, F(R) and used to create Tauc plots (**Figure 4**) with $[F(R)h\nu]^{1/2}$ for indirect band gap materials in agreement with some previous reports.[33, 45, 68] While both direct and indirect band gap analyses are found for polymeric carbon nitrides, ideal planar structures are predicted to have a direct band gap,[37] but structural defects from hydrogen forming NH bridges and layer buckling increase the likelihood that an indirect optical transition occurs that involves lattice vibrations. Indirect band gap estimates for these polymeric carbon nitrides from extrapolation of linear regions of the Tauc plot data yields $E_g$ values of 2.45, 2.35, 2.42, 2.62, and 2.65 eV for TCM-$C_3N_4$(P), TCM-$C_3N_4$(P/A), TCM-$C_3N_4$(T), MA-$C_3N_4$(T), and DCDA-$C_3N_4$(T), respectively. The larger and similar band gaps for the DCDA and melamine products are comparable to values reported for these light yellow colored carbon nitrides.[69] Direct band gap calculations on the DRS data yielded energies that were 0.2-0.3 eV larger than the indirect band gap values and similar difference has been noted by others.[70] A decrease in band gap from TCM-$C_3N_4$(P) to TCM-$C_3N_4$(P/A) observed here has been attributed to higher processing temperatures that may lead to a more fully condensed or packed carbon nitride structure with stronger heptazine-heptazine ring interactions.[12, 37, 70] The absorption edges of the darker orange colored TCM products are more diffuse and extend further into the visible region with absorbance continuing to ~700 nm. A second lower energy absorption event near 2 eV is also observed for the TCM-based carbon nitrides, which may arise from structural defects giving rise to intermediate band absorption. Similar lower energy absorption edges have been reported for high temperature synthesis or annealing of carbon nitrides, and are attributed to increasingly allowed transitions of non-bonding nitrogen (lone pair) electrons into $\pi^*$ orbitals in less planar or buckled structures.[10, 44, 71]

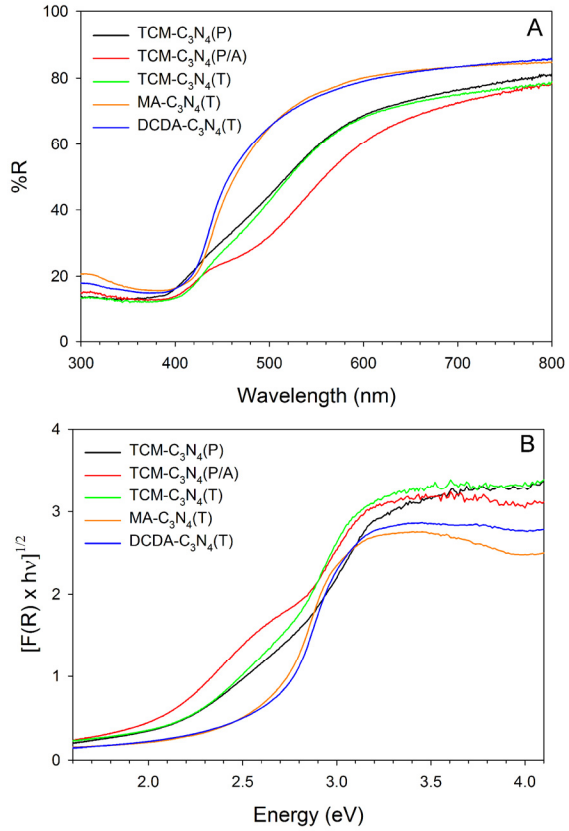


**Figure 4**. UV-vis DRS data for $C_3N_4$ products (A) reflectance data and (B) Tauc plots.

Polymeric carbon nitride materials show color, optical absorption, and emission differences that can track with their thermal processing history and structural ordering or degree of condensation.[12, 33, 44] The room-temperature photoluminescence (PL) of the three TCM-derived carbon nitride products show broad main emission near 460 nm (2.70 eV) with the 500 °C heated products showing increased intensity for a lower energy emission shoulder near 500 nm (2.48 eV) that tails out to ~600 nm (2.1 eV) (**Figure S7**). This decrease in luminescence intensity has been previously observed for higher processing temperatures.[44] The main emission peak for the annealed TCM-$C_3N_4$(P/A) product developed a slightly blue shifted shoulder relative to the original TCM-$C_3N_4$(P), but its low energy region near ~500 nm also became more pronounced. The direct to 500 °C TCM decomposition, TCM-$C_3N_4$(T), showed less intense emission and more lower energy emission near 500 nm. In the case of these disordered polymeric materials, lower emission intensities may be an indication of increased non-radiative charge carrier (electron/hole) recombination occurring that may negatively impact their use in catalysis. A

recent study clearly demonstrated that subtle variations in melamine-derived polymeric carbon nitride and its heptazine layer stacking interactions leads to significant changes in optical properties, for example a change from yellow to orange products as processing temperature increases from 500 to 700 °C.[12] The higher temperature orange carbon nitride, similar to our 500 °C treated TCM-$C_3N_4$ products, show increased absorption near 500 nm along with a main emission peak at 460 nm.[12, 71] Our previous work on sublimed carbon nitride films and powders yielded similarly broad PL emission that peaks in the 450 – 470 nm region.[26, 72-73]

**Photocatalytic dye oxidation studies**. The chemical robustness and optical absorption properties of polymeric carbon nitrides makes them attractive as photocatalysts. The oxidative photodegradation of methyl orange (MO) dye was performed in air using ball milled TCM-$C_3N_4$ and DCDA-$C_3N_4$ products. The photocatalytic oxidative breakdown of MO and other dyes using semiconducting photocatalysts is well studied and is often attributed to the generation of both hydroxyl and superoxide radicals which aid in the oxidation of the dye.[2, 61, 65] Atmospheric oxygen is reduced to superoxide using photogenerated conduction band electrons and corresponding valence band holes oxidize water to hydroxyl radicals. Both reactive oxygen species can then degrade the MO dye molecules. Initial photooxidation tests with TCM-$C_3N_4$(P) were performed in neutral conditions, however after the dark stir period, the dye solution for some samples changed to a darker red-orange color indicating an increase in solution acidity since MO is a pH indicator and its $\lambda_{max}$ changes when the solution pH is below 4. Residual HCl bound to the carbon nitride surface during synthesis in a high pressure Parr reactor may cause the dye indicator to change color. This is consistent with our previous work showing that suspensions of TCM-$C_3N_4$(P) in water reduced the pH from 7 to 3.[26] In order to ensure the dye absorption maximum did not change during the oxidation studies, MO dye experiments were performed in a pH 3 solution environment. The MO dye is very stable under UV light illumination in the absence of catalyst, staying above 95% of its initial concentration after two hours of UV exposure (**Figure 5A**). The dark adsorption of the dye onto the carbon nitride photocatalyst surfaces varied, with most being less than 10% except for TCM-$C_3N_4$(P), which adsorbed near 20% of the MO dye in solution. This may be due to adsorbed HCl on the TCM-$C_3N_4$(P) that affects its surface charge and attraction for the cationic MO dye. Carbon nitride samples prepared from the different methods performed similarly and degraded greater than 70% of the MO dye in two hours of UV illumination. Both TCM-$C_3N_4$(P) and DCDA-$C_3N_4$(T) completely degraded the dye at the two-hour illumination point. TCM-$C_3N_4$(P) appears slightly more active than DCDA-$C_3N_4$(T) but this difference may be due to differences in dark dye absorption. The linearized rates of each catalyst are compared in **Figure S8A** and rates are listed in the Figure 5 caption.

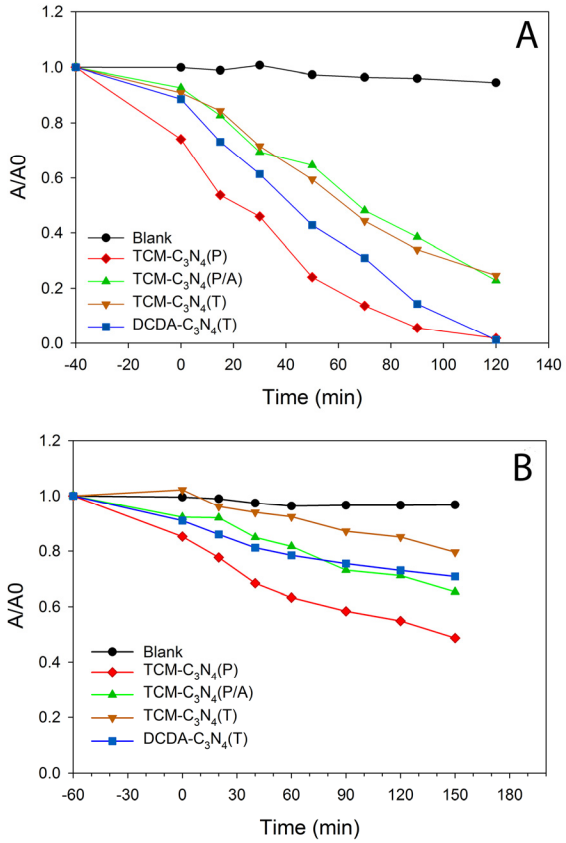


**Figure 5**. UV-vis photodegradation of MO dye under (A) UV light irradiation, (B) visible light irradiation. UV (visible) light rate constants ($min^{-1}$) for TCM-$C_3N_4$(P) 0.0242 (0.0037), TCM-$C_3N_4$(P/A) 0.0096 (0.0024), TCM-$C_3N_4$(T) 0.0112 (0.0015), and DCDA-$C_3N_4$(T) 0.0152 (0.0018).

Under visible light illumination, the carbon nitride photoactivity was lower than observed for unfiltered UV illumination (**Figure 5B**). The MO dye remained at 50-80% of its original concentration after 150 minutes of illumination. TCM-$C_3N_4$(P) still showed the highest dark dye surface adsorption, as well as degrading more dye at the end of each illumination period. The estimated rates based on **Figure S8B** for visible light degradation of MO shows that after accounting for the concentration loss due to dark adsorption, TCM-$C_3N_4$(P) still has the highest MO degradation rate for both visible (0.0037 $min^{-1}$) and UV light (0.024 $min^{-1}$). These rates are comparable to previously reported visible light MO degradation with carbon nitrides.[74] The approximate photon flux reaching the carbon nitride catalysts in the dye solution is 3.2 x $10^{17}$ photons $s^{-1}$ for UV light and 1.1 x $10^{17}$ photons $s^{-1}$ for visible light based on our previous work.[57] Based on the initial degradation rates, there is a loss of 3.05 x $10^{-4}$ dye molecules per UV/vis light photon above the band gap energy and 1.36 x $10^{-4}$ dye molecules per visible light photon. Given that the carbon nitride band gaps are in the near UV region, cutoff filters limit both flux intensity

and photons of appropriate wavelength for electron/hole formation necessary for MO photooxidation. In addition, effective photocatalysis requires that both electrons and holes be used effectively during irradiation to maintain charge neutrality in the carbon nitride photocatalyst. If defects form or degradation occurs in the carbon nitride network, this can also affect catalyst function. In an effort to examine the UV oxidative stability of the polymeric carbon nitrides used here, a sample of TCM-$C_3N_4$(P) was placed into an oxygen purged reactor and irradiated with UV light for up to four hours. Under these conditions, no changes were observed in the IR spectra of the product before and after UV exposure (**Figure S13**), particularly no evidence of ring oxidation with carbonyl formation. The orange carbon nitride color was also retained.

**Photocatalytic hydrogen evolution reactions**. In many previous hydrogen evolution studies with polymeric carbon nitride materials, the UV photodeposition of a noble metal co-catalyst is performed *in-situ*, followed by $H_2$ evolution analysis. This can lead to unknown solution environments or redox active metal species remaining in solution. We performed sequential metal (Pt, Pd, Ag) photodeposition and isolation in order to analyze the amount of metal *actually* deposited on the carbon nitride surface from the 1 wt% metal in solution. Metals photodeposited from the 1 wt% solutions were not detectable by XRD, but XPS identified the presence of each metal on the carbon nitride surface. The actual amount of surface deposited metal co-catalyst was determined by ICP-OES and the amounts Pt metal varied widely from ~0.13 to 0.5 wt% (**Table 2**). This shows that a nominally 1 wt% metal coated product may contain much less than that amount on its surface, which would leave the remaining metal cations in solution that can influence subsequent photocatalytic hydrogen evolution studies. In the current materials, the photoreduced metals on the surface likely interact with the carbon nitride at surface sites that are most able to provide photoexcited conduction band electrons.

Photocatalytic hydrogen evolution reactions with TCM-$C_3N_4$(P) [with and without a Pt co-catalyst] in the presence of a TEOA sacrificial oxidant were monitored in real-time using an RGA-MS system and four illumination and venting cycles shown in **Figure 6**. It was sometimes observed that the first cycle showed lower activity than the subsequent cycles. Venting the reactor after the first illumination cycle increased and stabilized the $H_2$ evolution rate for at least three additional one-hour cycles (*c.f.*, **Figure S10A**). This UV activating cycle was effective with as little as 10 minutes of UV illumination. The nature of this photoactivation step is unclear, but it may involve removal of a surface adsorbed species on platinum from the MeOH photodeposition by TEOA and UV illumination. The hydrogen evolution rates remain generally stable over several hour long cycles and the carbon nitride catalyst appears photostable, showing no visible changes to IR spectra after the extended UV photoreduction in aqueous TEOA.

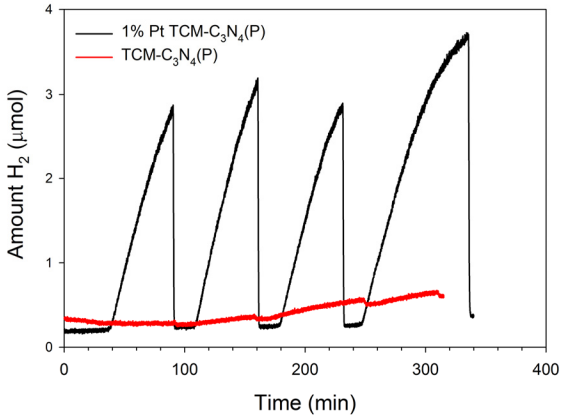


**Figure 6.** Four cycles of hydrogen production using 10 mg of milled TCM-$C_3N_4$(P) with and without 1 wt % nominal platinum loading (actual Pt is 0.39 wt%). Note the 4$^{th}$ cycle for the 1% Pt sample was run for 90 minutes to examine longer evolution times.

While rates for the degradation of methyl orange oxidation above were comparable for the TCM, DCDA, and MA derived carbon nitride photocatalysts, there were clear differences in the hydrogen production rates (**Table 2**), with DCDA-$C_3N_4$(T) having the highest mass averaged rate of 453 μmol $h^{-1}$ $g^{-1}$. Some of these $H_2$ evolution differences are likely due to catalyst surface area (DCDA-$C_3N_4$ highest for non-milled materials) and differing amounts of Pt photodeposited on the surface (TCM-$C_3N_4$(T) being lowest). Additionally any differences in structural ordering or defects for different precursor or thermal treatments may play important roles in influencing charge carrier formation and utilization in the proton reduction to $H_2$ photocatalytic process. As shown in the photoluminescence data, TCM-$C_3N_4$(P) had a higher emission (e-/hole recombination) intensity than TCM-$C_3N_4$(P/A). This could indicate faster recombination of charge carriers, which could reduce the efficiency of photocatalytic rate of hydrogen reduction. However the TCM-$C_3N_4$(T) product has the lowest PL intensity but also a lower $H_2$ rate than TCM-$C_3N_4$(P/A) and these samples have similar surface areas but much less Pt was photoreduced onto the TCM-$C_3N_4$(T) surface. There is a notable ~6x improvement in $H_2$ evolution rates upon milling as-synthesized TCM-$C_3N_4$(P) (~2x surface area and similar amount of Pt deposited), but much less improvement when treating TCM-$C_3N_4$(P/A) in the same manner (see **Table 2**) even when accompanied by higher Pt deposition amounts. There are no clear single property trends (either surface area, % Pt deposition, or PL emission) that explain all of the $H_2$ evolution differences in Table 2. Quantum yields (QY%) for each catalyst are also presented in **Table 2**. These values are lower compared to other similar reports,[66, 75] but our values were calculated for the total incident photon flux emitted from the Hg lamp with energies greater than the carbon nitride band gap. A comparison to several previously reported bulk

carbon nitride $H_2$ evolution photocatalysts is shown in **Table S4**. Most comparable is a rate of 200 μmol $h^{-1}$ $g^{-1}$ for carbon nitride prepared from DCDA under illumination at wavelengths >300 nm.[76] The thermally heated and milled TCM-$C_3N_4$ products show similar $H_2$ evolution activity, however our current study's analogous DCDA comparison material exhibits more than twice the activity of this previous report.

**Table 2**. Metal co-catalyst content and hydrogen evolution rates for carbon nitride samples

| **Sample** | **Target wt% M (ICP wt%)** | **$H_2$ Rate (μmol $h^{-1}$ $g^{-1}$)[1]** | **QY%** |
|---|---|---|---|
| **TCM-$C_3N_4$(P) - milled** | None | 9 (3) | 0.01 |
| **TCM-$C_3N_4$(P)** | 1% Pt (0.39) | 43 (4) | 0.03 |
| **TCM-$C_3N_4$(P) - milled** | 1% Pt (0.40) | 260 (30) | 0.17 |
| **TCM-$C_3N_4$(P/A)** | 1% Pt (0.28) | 153 (35) | 0.10 |
| **TCM-$C_3N_4$(P/A) - milled** | 1% Pt (0.49) | 193 (12) | 0.12 |
| | | | |
| **TCM-$C_3N_4$(T)** | 1% Pt (0.13) | 68 (8) | 0.04 |
| **DCDA-$C_3N_4$(T)** | 1% Pt (0.33) | 453 (67) | 0.29 |
| **MA-$C_3N_4$(T)** | 1% Pt (0.28) | 283 (50) | 0.18 |
| | | | |
| **TCM-$C_3N_4$(P) - milled** | 1% Pd (0.37) | 127 (15) | 0.08 |
| **TCM-$C_3N_4$(P) - milled** | 1% Ag (0.06) | 63 (10) | 0.04 |

1) Average rates for four cycles reported with standard deviation in parentheses.

The effect of the co-catalyst metal was also studied and moving from Ag<Pd<Pt resulted in roughly doubled hydrogen evolution rates for nominally 1 wt% metal deposition (**Table 2**). It is worth noting that a TCM-$C_3N_4$(P) sample loaded with Pd at similar levels as Pt, showed ~50% of the activity of the more expensive Pt catalyst. The difference in activities for these metals shows similar trends to previously reported data for other precious metal co-catalysts on cyanamide based products.[77] At higher deposition targets of ~2 wt%, more metal is deposited on the carbon nitride surface and broad nanoscale (~4-9 nm crystallite sizes) metal peaks are observed by XRD (**Figure S9**). For example, increasing the Pt solution concentration to 2 wt% for a TCM-$C_3N_4$(T) sample increased the metal loading to 0.46 wt% Pt on the carbon nitride surface (**Table S3**), but its mass averaged HER was ~40 μmol $h^{-1}$ $g^{-1}$, similar to that for the nominally 1 wt% sample in **Table 2**. The variability of actual metal deposited on different carbon nitride structures observed here (and corresponding differences in HER photocatalytic activity) highlights the importance of performing a quantitative metals analysis on the exact carbon nitride samples used for catalytic studies to allow for useful comparisons across different literature reports.

**Photocatalysis and band comparisons.** As noted above the extrapolated indirect band gap absorptions (HOMO-LUMO) for the TCM derived $C_3N_4$ network structures are ~0.3 eV lower than that for DCDA or

MA products. In addition, low energy valence band spectra from XPS shows that the TCM products have valence band onset levels near 1.4-1.9 eV (**Figure S11**), which is similar to those reported for DCDA and MA derived $C_3N_4$.[78-79] Combining the $E_g$ and VB results leads to approximate simplified energy diagrams for TCM derived $C_3N_4$ materials (**Figure 7**). Even though there are subtle variations in the band gaps and conduction band positions, the TCM-$C_3N_4$ products are still in a position where the $2H^+ \rightarrow H_2$ reduction is possible. As expected, the deposition of Pt onto the TCM-$C_3N_4$ surface leads to valence band electron emission moving to near 0 eV, consistent with facile electron ejection from the surface-deposited metal (**Figure S11D**). This would also place Pt metal states below the $C_3N_4$ conduction band to readily accept photoexcited electrons from the CB for subsequent use in surface proton reduction. The apparent lower structure ordering of the TCM-$C_3N_4$(T) product versus TCM-$C_3N_4$(P) product may affect the energy levels of orbitals that make up its higher energy bonding states, leading to higher energy VB levels. This structural disorder for TCM-$C_3N_4$(T) may affect the lower photocatalytic activity for both Pt metal deposition and hydrogen production. It is expected that in these non-crystalline polymeric carbon nitride structures, solution photodeposition of metal co-catalysts will be very dependent on accessible surface structures that can serve as "antennas" to shuttle photoexcited conduction band electrons from carbon nitride orbitals to the Pt cations for surface reduction. These deposited metal regions are then likely the major reducing sites for subsequent $H^+ \rightarrow H_2$ photoreduction reactions. As noted earlier, tuning and controlling defects in polymeric carbon nitrides can greatly influence its catalytic activity.[51-53]

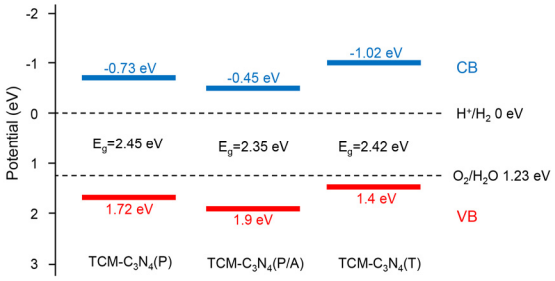


**Figure 7.** Generalized band structure diagram of TCM-$C_3N_4$(P), TCM-$C_3N_4$(P/A), and TCM-$C_3N_4$(T) from UV-vis absorption and valence band emission data.

## Conclusions

This work describes the preparation of semiconducting polymeric carbon nitride networks from the rapid and facile decomposition of a trichloromelamine (TCM) precursor. The chemical and structural properties are very similar to related materials synthesized by thermal processing of DCDA or melamine precursors. The low temperature TCM decomposition presents several potential advantages of quick carbon nitride growth and the possibility to form composites or infiltrated structures using other materials

that may be sensitive to the higher synthesis temperatures required for typical carbon nitride precursors. Rapid self-heating from this triazine precursor leads to effective ring expansion into heptazine-based carbon nitride ($C_3N_{4+x}H_y$) networks with several hundred nanometer-sized plate or sheet-like morphologies, but only a few nanometer of interlayer (heptazine-heptazine interactions) ordering. Further tuning of the decomposition to increase chlorine residues on the carbon nitride may aid future functionalization of the carbon nitride and can positively impact interaction with a Pt cocatalyst.[52] Notable differences in TCM-$C_3N_4$ products as compared to DCDA or melamine carbon nitrides are a darker orange product color and smaller band gap but similar luminescent emission that can vary based on subtle chemical and structural ordering differences that occur during synthesis. TCM-$C_3N_4$ photocatalytic oxidative degradation of methyl orange dye was comparable or exceeding that of DCDA-$C_3N_4$. Photocatalytic hydrogen evolution rates for TCM-$C_3N_4$ materials approach those from DCDA and melamine precursors, with differences likely influenced by a combination of surface area, and metal co-catalyst content, optical absorption properties, and structural ordering. Since polymeric carbon nitrides are non-crystalline network structures, they can vary in subtle but important structural and electronic ways, and so careful attention should be paid to analysis of the actual amount of metal co-catalyst deposition on catalytically assessable surface sites as it may vary greatly for different $C_3N_4$ structures, which can influence resulting catalytic properties.

**Acknowledgements**

The authors gratefully acknowledge partial funding support from the National Science Foundation (CHE-0957555) and the ACS Petroleum Research Fund (54110-ND10) and a graduate fellowship (A.T.M.) from the Department of Education's Graduate Assistance in Areas of National Need (GAANN) program (P200A150065). We thank Dr. George Crull (University of Iowa, Assistant Director of NMR Facility) for the collection of $^{13}C$ CP-MAS NMR data. Dr. Sylvia Lee (University of Iowa Central Microscopy Research Facility) is gratefully acknowledged for assistance with XPS acquisition and analysis and similarly Majid Nada's (University of Iowa, Larsen group) assistance with BET and ICP analysis is much appreciated.

**Supporting Information.** Gas phase IR of TCM decomposition byproducts, TGA-DTA of TCM precursor and $C_3N_4$ products, XPS and $^{13}C$ NMR data, additional SEM images, XRD data on metal deposited products, table of ICP-OES results, examples of $H_2$ data from RGA-MS, XPS valence band spectra, tables of $^{13}C$ NMR and $H_2$ evolution comparisons, nitrogen adsorption/desorption isotherms, IR result for TCM-$C_3N_4$(P) exposed to UV/$O_2$ for several hours.

**References**


1. Zheng, Y.; Lin, L.; Wang, B.; Wang, X. Graphitic carbon nitride polymers toward sustainable photoredox catalysis. *Angew. Chem. Int. Ed.* **2015,** *54* (44), 12868-84.
2. Mamba, G.; Mishra, A. K. Graphitic carbon nitride (g-C3N4) nanocomposites: A new and exciting generation of visible light driven photocatalysts for environmental pollution remediation. *Appl. Catal. B-Environ.* **2016,** *198*, 347-377.
3. Wang, X.; Blechert, S.; Antonietti, M. Polymeric graphitic carbon nitride for heterogeneous photocatalysis. *ACS Catal.* **2012,** *2* (8), 1596-1606.
4. Wang, Y.; Wang, X.; Antonietti, M. Polymeric graphitic carbon nitride as a heterogeneous organocatalyst: From photochemistry to multipurpose catalysis to sustainable chemistry. *Angew. Chem. Int. Ed.* **2012,** *51* (1), 68-89.
5. Zhu, J.; Xiao, P.; Li, H.; Carabineiro, S. A. Graphitic carbon nitride: Synthesis, properties, and applications in catalysis. *ACS Appl. Mater. Interfaces* **2014,** *6* (19), 16449-65.
6. Kessler, F. K.; Zheng, Y.; Schwarz, D.; Merschjann, C.; Schnick, W.; Wang, X.; Bojdys, M. J. Functional carbon nitride materials — design strategies for electrochemical devices. *Nature Reviews Materials* **2017,** *2* (6), 17030.
7. Kroke, E.; Schwarz, M. Novel group 14 nitrides. *Coordination Chemistry Reviews* **2004,** *248* (5-6), 493-532.
8. Wen, J.; Xie, J.; Chen, X.; Li, X. A review on g-C3N4 -based photocatalysts. *Appl. Surf. Sci.* **2017,** *391*, 72-123.
9. Naseri, A.; Samadi, M.; Pourjavadi, A.; Moshfegh, A. Z.; Ramakrishna, S. Graphitic carbon nitride (g-C3N4)-based photocatalysts for solar hydrogen generation: Recent advances and future development directions. *J. Mater. Chem. A* **2017,** *5* (45), 23406-23433.
10. Miller, T. S.; Jorge, A. B.; Suter, T. M.; Sella, A.; Cora, F.; McMillan, P. F. Carbon nitrides: Synthesis and characterization of a new class of functional materials. *Phys Chem Chem Phys* **2017,** *19* (24), 15613-15638.
11. Han, Q.; Cheng, Z.; Wang, B.; Zhang, H.; Qu, L. Significant enhancement of visible-light-driven hydrogen evolution by structure regulation of carbon nitrides. *ACS Nano* **2018**.
12. Li, X.; Melissen, S. T. A. G.; Le Bahers, T.; Sautet, P.; Masters, A. F.; Steinmann, S. N.; Maschmeyer, T. Shining light on carbon nitrides: Leveraging temperature to understand optical gap variations. *Chem. Mater.* **2018,** *30* (13), 4253-4262.
13. Franklin, E. C. The ammono carbonic acids. *J. Am. Chem. Soc.* **1922,** *44*, 486-509.
14. Thomas, A.; Fischer, A.; Goettmann, F.; Antonietti, M.; Müller, J.-O.; Schlögl, R.; Carlsson, J. M. Graphitic carbon nitride materials: Variation of structure and morphology and their use as metal-free catalysts. *J. Mater. Chem.* **2008,** *18* (41), 4893.
15. Holst, J. R.; Gillan, E. G. From triazines to heptazines: Deciphering the local structure of amorphous nitrogen-rich carbon nitride materials. *J. Am. Chem. Soc.* **2008,** *130* (23), 7373-9.
16. Ong, W. J.; Tan, L. L.; Ng, Y. H.; Yong, S. T.; Chai, S. P. Graphitic carbon nitride (g-C3N4)-based photocatalysts for artificial photosynthesis and environmental remediation: Are we a step closer to achieving sustainability? *Chemical reviews* **2016,** *116* (12), 7159-329.
17. Kumar, S.; Kumar, B.; Surendar, T.; Shanker, V. G-C3N4/NaTaO3 organic–inorganic hybrid nanocomposite: High-performance and recyclable visible light driven photocatalyst. *Mater. Res. Bull.* **2014,** *49*, 310-318.
18. Zhang, Y.; Thomas, A.; Antonietti, M.; Wang, X. Activation of carbon nitride solids by protonation: Morphology changes, enhanced ionic conductivity, and photoconduction experiments. *J. Am. Chem. Soc.* **2009,** *131* (1), 50-1.

19. Lan, H.; Li, L.; An, X.; Liu, F.; Chen, C.; Liu, H.; Qu, J. Microstructure of carbon nitride affecting synergetic photocatalytic activity: Hydrogen bonds vs. Structural defects. *Appl. Catal. B-Environ.* **2017,** *204*, 49-57.
20. Komatsu, T. The first synthesis and characterization of cyameluric high polymers. *Macromol. Chem. Phys.* **2001,** *202* (1), 19-25.
21. Komatsu, T. Prototype carbon nitrides similar to the symmetric triangular form of melon. *J. Mater. Chem.* **2001,** *11* (3), 802-805.
22. Lotsch, B. V.; Doblinger, M.; Sehnert, J.; Seyfarth, L.; Senker, J.; Oeckler, O.; Schnick, W. Unmasking melon by a complementary approach employing electron diffraction, solid-state NMR spectroscopy, and theoretical calculations-structural characterization of a carbon nitride polymer. *Chemistry* **2007,** *13* (17), 4969-80.
23. Jurgens, B.; Irran, E.; Senker, J.; Kroll, P.; Muller, H.; Schnick, W. Melem (2,5,8-triamino-tri-s-triazine), an important intermediate during condensation of melamine rings to graphitic carbon nitride: Synthesis, structure determination by x-ray powder diffractometry, solid-state NMR, and theoretical studies. *J. Am. Chem. Soc.* **2003,** *125* (34), 10288-300.
24. Dong, G.; Zhang, L. Porous structure dependent photoreactivity of graphitic carbon nitride under visible light. *J. Mater. Chem.* **2012,** *22* (3), 1160.
25. Fina, F.; Callear, S. K.; Carins, G. M.; Irvine, J. T. S. Structural investigation of graphitic carbon nitride via XRD and neutron diffraction. *Chem. Mater.* **2015,** *27* (7), 2612-2618.
26. Miller, D. R.; Wang, J. J.; Gillan, E. G. Rapid, facile synthesis of nitrogen-rich carbon nitride powders. *J. Mater. Chem.* **2002,** *12* (8), 2463-2469.
27. Schwarzer, A.; Saplinova, T.; Kroke, E. Tri-s-triazines (s-heptazines)—from a "mystery molecule" to industrially relevant carbon nitride materials. *Coordination Chemistry Reviews* **2013,** *257* (13-14), 2032-2062.
28. Horvath-Bordon, E.; Kroke, E.; Svoboda, I.; Fuess, H.; Riedel, R.; Neeraj, S.; Cheetham, A. K. Alkalicyamelurates, m3[c6n7o3].Xh2o, m = li, na, k, rb, cs: Uv-luminescent and thermally very stable ionic tri-s-triazine derivatives. *Dalton transactions* **2004,** (22), 3900-8.
29. Kouvetakis, J.; Bandari, A.; Todd, M.; Wilkens, B.; Cave, N. Novel synthetic routes to carbon-nitrogen thin-films. *Chem. Mater.* **1994,** *6* (6), 811-814.
30. Algara-Siller, G.; Severin, N.; Chong, S. Y.; Bjorkman, T.; Palgrave, R. G.; Laybourn, A.; Antonietti, M.; Khimyak, Y. Z.; Krasheninnikov, A. V.; Rabe, J. P.; Kaiser, U.; Cooper, A. I.; Thomas, A.; Bojdys, M. J. Triazine-based graphitic carbon nitride: A two-dimensional semiconductor. *Angew Chem Int Ed Engl* **2014,** *53* (29), 7450-5.
31. Cui, Y.; Ding, Z.; Liu, P.; Antonietti, M.; Fu, X.; Wang, X. Metal-free activation of h2o2 by g-C3N4 under visible light irradiation for the degradation of organic pollutants. *Phys. Chem. Chem. Phys.* **2012,** *14* (4), 1455-62.
32. Ishida, Y.; Chabanne, L.; Antonietti, M.; Shalom, M. Morphology control and photocatalysis enhancement by the one-pot synthesis of carbon nitride from preorganized hydrogen-bonded supramolecular precursors. *Langmuir* **2014,** *30* (2), 447-51.
33. Dong, F.; Zhao, Z.; Xiong, T.; Ni, Z.; Zhang, W.; Sun, Y.; Ho, W. K. In situ construction of g-C3N4/g-C3N4 metal-free heterojunction for enhanced visible-light photocatalysis. *ACS Appl Mater Interfaces* **2013,** *5* (21), 11392-401.
34. Kiskan, B.; Zhang, J.; Wang, X.; Antonietti, M.; Yagci, Y. Mesoporous graphitic carbon nitride as a heterogeneous visible light photoinitiator for radical polymerization. *ACS Macro Lett.* **2012,** *1* (5), 546-549.

35. Su, F.; Mathew, S. C.; Lipner, G.; Fu, X.; Antonietti, M.; Blechert, S.; Wang, X. Mpg-C3N4-catalyzed selective oxidation of alcohols using O2 and visible light. *J. Am. Chem. Soc.* **2010,** *132* (46), 16299-301.
36. Meyer, A. U.; Lau, V. W.-h.; König, B.; Lotsch, B. V. Photocatalytic oxidation of sulfinates to vinyl sulfones with cyanamide-functionalised carbon nitride. *Eur. J. Org. Chem.* **2017,** *2017* (15), 2179-2185.
37. Wang, X.; Maeda, K.; Thomas, A.; Takanabe, K.; Xin, G.; Carlsson, J. M.; Domen, K.; Antonietti, M. A metal-free polymeric photocatalyst for hydrogen production from water under visible light. *Nature materials* **2009,** *8* (1), 76-80.
38. Wang, X.; Maeda, K.; Chen, X.; Takanabe, K.; Domen, K.; Hou, Y.; Fu, X.; Antonietti, M. Polymer semiconductors for artificial photosynthesis: Hydrogen evolution by mesoporous graphitic carbon nitride with visible light. *J. Am. Chem. Soc.* **2009,** *131* (5), 1680-1.
39. Zhang, G.; Zhang, J.; Zhang, M.; Wang, X. Polycondensation of thiourea into carbon nitride semiconductors as visible light photocatalysts. *J. Mater. Chem.* **2012,** *22* (16), 8083.
40. Shalom, M.; Gimenez, S.; Schipper, F.; Herraiz-Cardona, I.; Bisquert, J.; Antonietti, M. Controlled carbon nitride growth on surfaces for hydrogen evolution electrodes. *Angew Chem Int Ed Engl* **2014,** *53* (14), 3654-8.
41. Chen, X.; Jun, Y.-S.; Takanabe, K.; Maeda, K.; Domen, K.; Fu, X.; Antonietti, M.; Wang, X. Ordered mesoporous sba-15 type graphitic carbon nitride: A semiconductor host structure for photocatalytic hydrogen evolution with visible light. *Chem. Mater.* **2009,** *21* (18), 4093-4095.
42. Goettmann, F.; Fischer, A.; Antonietti, M.; Thomas, A. Chemical synthesis of mesoporous carbon nitrides using hard templates and their use as a metal-free catalyst for friedel-crafts reaction of benzene. *Angew. Chem. Int. Ed.* **2006,** *45* (27), 4467-71.
43. Niu, P.; Zhang, L.; Liu, G.; Cheng, H.-M. Graphene-like carbon nitride nanosheets for improved photocatalytic activities. *Adv. Funct. Mater.* **2012,** *22* (22), 4763-4770.
44. Cao, Y.; Zhang, Z.; Long, J.; Liang, J.; Lin, H.; Lin, H.; Wang, X. Vacuum heat-treatment of carbon nitride for enhancing photocatalytic hydrogen evolution. *J. Mater. Chem. A* **2014,** *2* (42), 17797-17807.
45. Zhou, M.; Hou, Z.; Zhang, L.; Liu, Y.; Gao, Q.; Chen, X. N/n junctioned g-C3N4 for enhanced photocatalytic H2 generation. *Sustainable Energy & Fuels* **2017,** *1* (2), 317-323.
46. Zhang, J.; Zhang, G.; Chen, X.; Lin, S.; Mohlmann, L.; Dolega, G.; Lipner, G.; Antonietti, M.; Blechert, S.; Wang, X. Co-monomer control of carbon nitride semiconductors to optimize hydrogen evolution with visible light. *Angew Chem Int Ed Engl* **2012,** *51* (13), 3183-7.
47. Huang, D.; Yan, X.; Yan, M.; Zeng, G.; Zhou, C.; Wan, J.; Cheng, M.; Xue, W. Graphitic carbon nitride-based heterojunction photoactive nanocomposites: Applications and mechanism insight. *ACS Appl Mater Interfaces* **2018,** *10* (25), 21035-21055.
48. He, K.; Xie, J.; Liu, Z.-Q.; Li, N.; Chen, X.; Hu, J.; Li, X. Multi-functional ni3c cocatalyst/g-C3N4 nanoheterojunctions for robust photocatalytic H2 evolution under visible light. *J. Mater. Chem. A* **2018,** *6* (27), 13110-13122.
49. He, K.; Xie, J.; Li, M.; Li, X. In situ one-pot fabrication of g-c 3 n 4 nanosheets/NiS cocatalyst heterojunction with intimate interfaces for efficient visible light photocatalytic h 2 generation. *Applied Surface Science* **2018,** *430*, 208-217.
50. Fu, J. W.; Yu, J. G.; Jiang, C. J.; Cheng, B. G-C3N4-based heterostructured photocatalysts. *Adv. Energy Mater.* **2018,** *8* (3), 1701503.

51. Botari, T.; Huhn, W. P.; Lau, V. W.-h.; Lotsch, B. V.; Blum, V. Thermodynamic equilibria in carbon nitride photocatalyst materials and conditions for the existence of graphitic carbon nitride g-C3N4. *Chem. Mater.* **2017,** *29* (10), 4445-4453.
52. Lau, V. W.-h.; Yu, V. W.-z.; Ehrat, F.; Botari, T.; Moudrakovski, I.; Simon, T.; Duppel, V.; Medina, E.; Stolarczyk, J. K.; Feldmann, J.; Blum, V.; Lotsch, B. V. Urea-modified carbon nitrides: Enhancing photocatalytic hydrogen evolution by rational defect engineering. *Adv. Energy Mater.* **2017,** *7* (12), 1602251.
53. Lau, V. W.; Moudrakovski, I.; Botari, T.; Weinberger, S.; Mesch, M. B.; Duppel, V.; Senker, J.; Blum, V.; Lotsch, B. V. Rational design of carbon nitride photocatalysts by identification of cyanamide defects as catalytically relevant sites. *Nat Commun* **2016,** *7*, 12165.
54. Bennett, A. E.; Rienstra, C. M.; Auger, M.; Lakshmi, K. V.; Griffin, R. G. Heteronuclear decoupling in rotating solids. *J. Chem. Phys.* **1995,** *103* (16), 6951-6958.
55. Metz, G.; Wu, X. L.; Smith, S. O. Ramped-amplitude cross polarization in magic-angle-spinning NMR. *Journal of Magnetic Resonance, Series A* **1994,** *110* (2), 219-227.
56. Barich, D. H.; Gorman, E. M.; Zell, M. T.; Munson, E. J. 3-methylglutaric acid as a 13c solid-state NMR standard. *Solid State Nucl Magn Reson* **2006,** *30* (3-4), 125-9.
57. Montoya, A. T.; Gillan, E. G. Enhanced photocatalytic hydrogen evolution from transition-metal surface-modified TiO2. *ACS Omega* **2018,** *3* (3), 2947-2955.
58. Lotsch, B. V.; Schnick, W. New light on an old story: Formation of melam during thermal condensation of melamine. *Chemistry* **2007,** *13* (17), 4956-68.
59. Gillan, E. G. Synthesis of nitrogen-rich carbon nitride networks from an energetic molecular azide precursor. *Chem Mater* **2000,** *12* (12), 3906-3912.
60. Zheng, W.; Wong, N.-B.; Zhou, G.; Liang, X.; Li, J.; Tian, A. Theoretical study of tri-s-triazine and some of its derivatives. *New J. Chem.* **2004,** *28* (2), 275.
61. Yan, S. C.; Li, Z. S.; Zou, Z. G. Photodegradation performance of g-C3N4 fabricated by directly heating melamine. *Langmuir* **2009,** *25* (17), 10397-401.
62. Bojdys, M. J.; Muller, J. O.; Antonietti, M.; Thomas, A. Ionothermal synthesis of crystalline, condensed, graphitic carbon nitride. *Chemistry* **2008,** *14* (27), 8177-82.
63. Miller, D. R.; Holst, J. R.; Gillan, E. G. Nitrogen-rich carbon nitride network materials via the thermal decomposition of 2,5,8-triazido-s-heptazine. *Inorganic chemistry* **2007,** *46* (7), 2767-74.
64. Miller, D. R.; Swenson, D. C.; Gillan, E. G. Synthesis and structure of 2,5,8-triazido-s-heptazine: An energetic and luminescent precursor to nitrogen-rich carbon nitrides. *J Am Chem Soc* **2004,** *126* (17), 5372-3.
65. Chen, Z.; Sun, P.; Fan, B.; Liu, Q.; Zhang, Z.; Fang, X. Textural and electronic structure engineering of carbon nitride via doping with π-deficient aromatic pyridine ring for improving photocatalytic activity. *Appl. Catal. B-Environ.* **2015,** *170-171*, 10-16.
66. Rahman, M. Z.; Tapping, P. C.; Kee, T. W.; Smernik, R.; Spooner, N.; Moffatt, J.; Tang, Y.; Davey, K.; Qiao, S.-Z. A benchmark quantum yield for water photoreduction on amorphous carbon nitride. *Adv. Funct. Mater.* **2017,** *27* (39), 1702384.
67. Kruk, M.; Jaroniec, M. Gas adsorption characterization of ordered organic−inorganic nanocomposite materials. *Chem Mater* **2001,** *13* (10), 3169-3183.
68. Dong, F.; Wu, L.; Sun, Y.; Fu, M.; Wu, Z.; Lee, S. C. Efficient synthesis of polymeric g-C3N4 layered materials as novel efficient visible light driven photocatalysts. *J. Mater. Chem.* **2011,** *21* (39), 15171.

69. Cao, S.; Low, J.; Yu, J.; Jaroniec, M. Polymeric photocatalysts based on graphitic carbon nitride. *Adv. Mater.* **2015,** *27* (13), 2150-76.
70. Tyborski, T.; Merschjann, C.; Orthmann, S.; Yang, F.; Lux-Steiner, M. C.; Schedel-Niedrig, T. Tunable optical transition in polymeric carbon nitrides synthesized via bulk thermal condensation. *J. Phys.: Condens. Matter* **2012,** *24* (16), 162201.
71. Jorge, A. B.; Martin, D. J.; Dhanoa, M. T. S.; Rahman, A. S.; Makwana, N.; Tang, J.; Sella, A.; Corà, F.; Firth, S.; Darr, J. A.; McMillan, P. F. H2 and O2 evolution from water half-splitting reactions by graphitic carbon nitride materials. *J. Phys. Chem. C* **2013,** *117* (14), 7178-7185.
72. Wang, J.; Miller, D. R.; Gillan, E. G. Photoluminescent carbon nitride films grown by vapor transport of carbon nitride powders. *Chemical communications* **2002,** (19), 2258-9.
73. Wang, J.; Gillan, E. G. Low-temperature deposition of carbon nitride films from a molecular azide, (c3n3)(n3)3. *Thin Solid Films* **2002,** *422* (1-2), 62-68.
74. Jiang, L.; Yuan, X.; Zeng, G.; Chen, X.; Wu, Z.; Liang, J.; Zhang, J.; Wang, H.; Wang, H. Phosphorus- and sulfur-codoped g-C3N4: Facile preparation, mechanism insight, and application as efficient photocatalyst for tetracycline and methyl orange degradation under visible light irradiation. *ACS Sustainable Chem. Eng.* **2017,** *5* (7), 5831-5841.
75. Chen, Z.; Fan, T.-T.; Yu, X.; Wu, Q.-L.; Zhu, Q.-H.; Zhang, L.-Z.; Li, J.-H.; Fang, W.-P.; Yi, X.-D. Gradual carbon doping of graphitic carbon nitride towards metal-free visible light photocatalytic hydrogen evolution. *J. Mater. Chem. A* **2018,** *6* (31), 15310-15319.
76. Liu, G.; Niu, P.; Sun, C.; Smith, S. C.; Chen, Z.; Lu, G. Q.; Cheng, H. M. Unique electronic structure induced high photoreactivity of sulfur-doped graphitic C3N4. *J. Am. Chem. Soc.* **2010,** *132* (33), 11642-8.
77. Maeda, K.; Wang, X.; Nishihara, Y.; Lu, D.; Antonietti, M.; Domen, K. Photocatalytic activities of graphitic carbon nitride powder for water reduction and oxidation under visible light. *J. Phys. Chem. C* **2009,** *113* (12), 4940-4947.
78. Chang, F.; Li, C. L.; Luo, J. R.; Xie, Y. C.; Deng, B. Q.; Hu, X. F. Enhanced visible-light-driven photocatalytic performance of porous graphitic carbon nitride. *Appl. Surf. Sci.* **2015,** *358*, 270-277.
79. Xiao, T.; Tang, Z.; Yang, Y.; Tang, L.; Zhou, Y.; Zou, Z. In situ construction of hierarchical WO3 /g-C3N4 composite hollow microspheres as a z-scheme photocatalyst for the degradation of antibiotics. *Appl. Catal. B-Environ.* **2018,** *220*, 417-428.

**Table of Contents/Abstract Graphic**

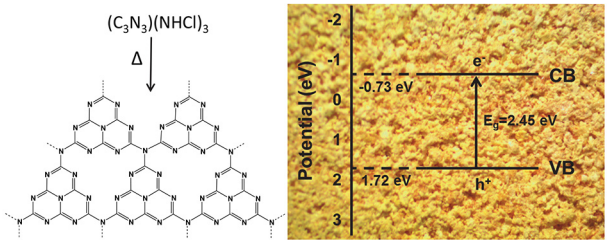

Supporting Information for:

**Photocatalytic Carbon Nitride Materials with Nanoscale Features Synthesized from the Rapid and Low-Temperature Decomposition of Trichloromelamine**

Anthony T. Montoya and Edward G. Gillan*

Department of Chemistry, University of Iowa, Iowa City, Iowa 52242

Email: edward-gillan@uiowa.edu ORCID (Edward Gillan): 0000-0002-2047-0929

Supporting Information contents:

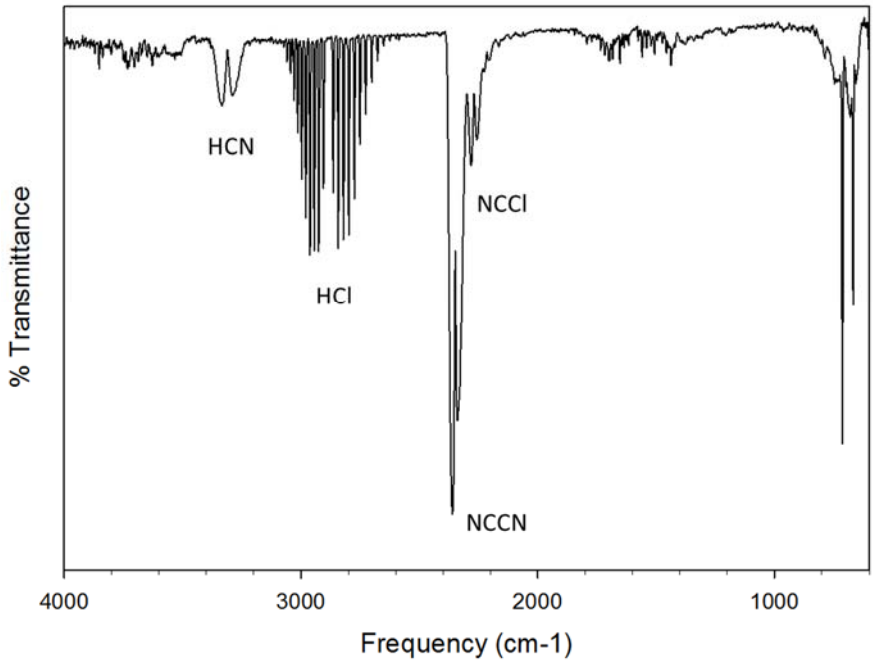


**Figure S1**. Gas phase FT-IR spectrum of byproducts from TCM-$C_3N_4$(T) reaction sampled immediately after TCM exothermic decomposition occurred.

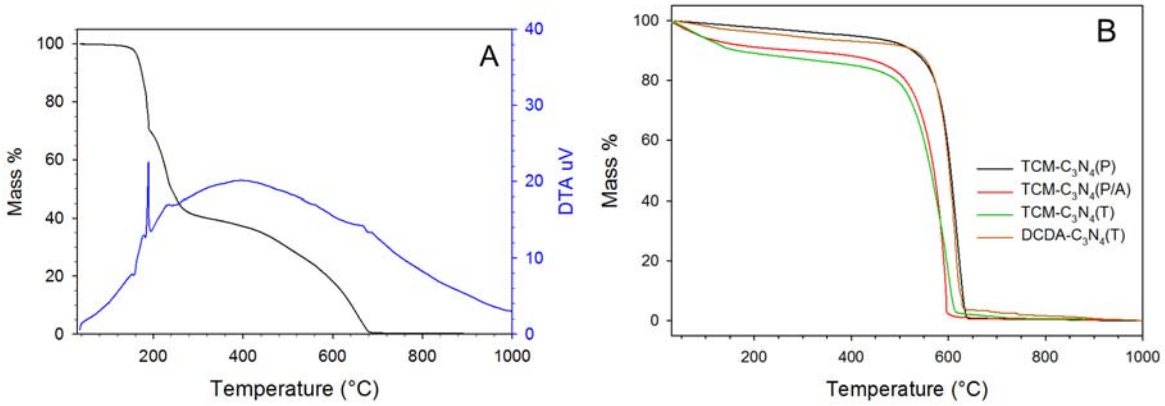


**Figure S2**. (A) TGA-DTA plots of the decomposition of TCM under argon flow and (B) TGA overlays of TCM-$C_3N_4$(P), TCM-$C_3N_4$(T), and DCDA-$C_3N_4$(T) under air flow.

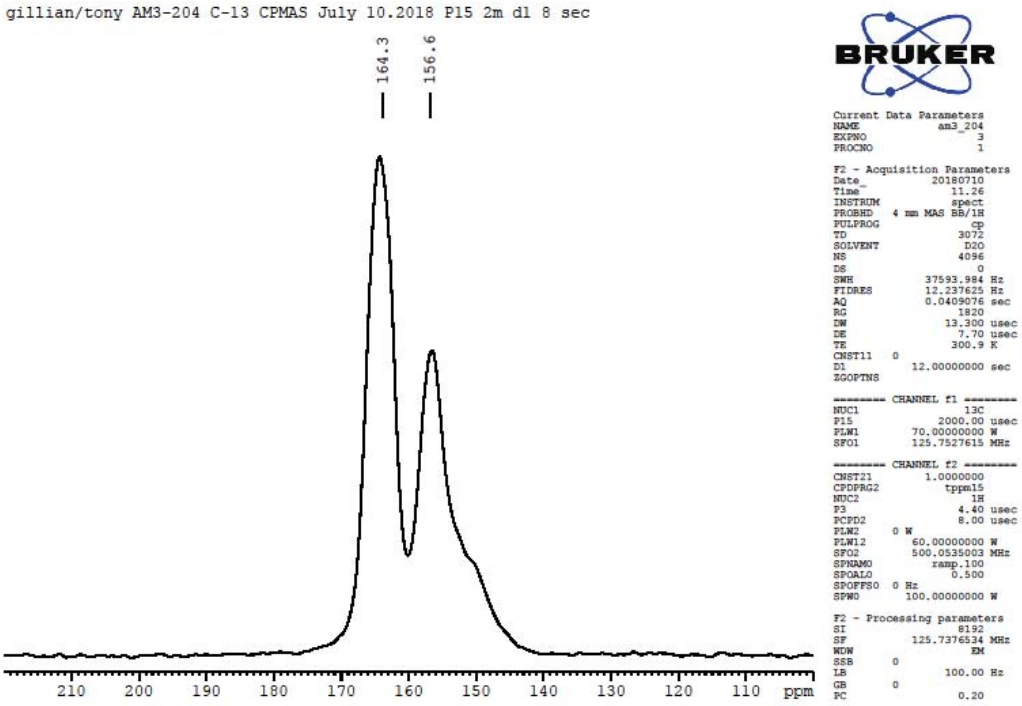


**Figure S3A**. CPMAS $^{13}C$ NMR of TCM-$C_3N_4$(P) sample.

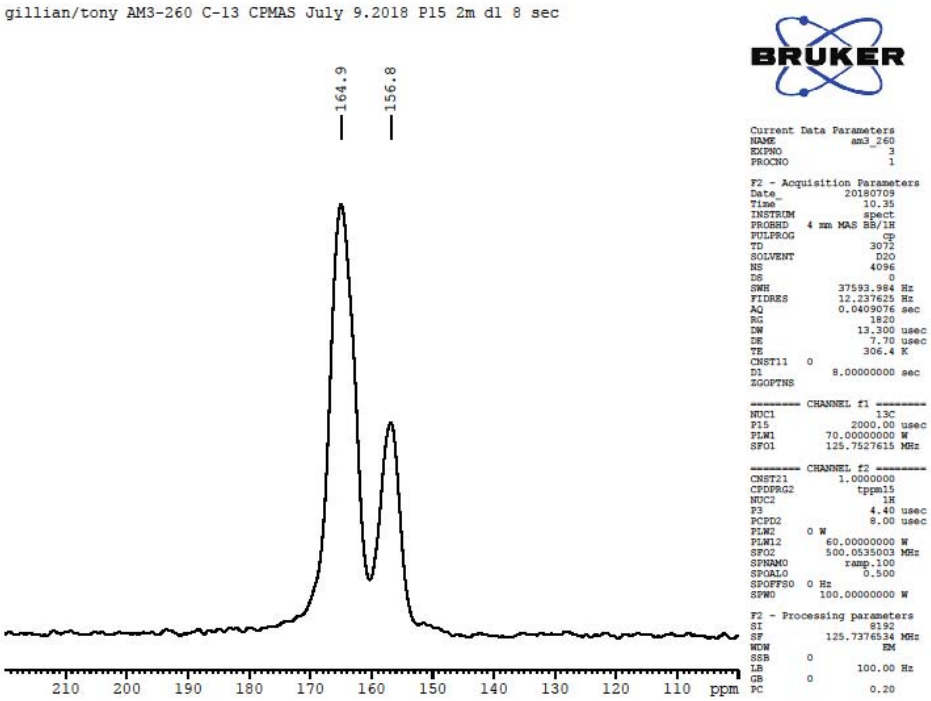


**Figure S3B**. CPMAS $^{13}C$ NMR of TCM-$C_3N_4$(P/A) sample.

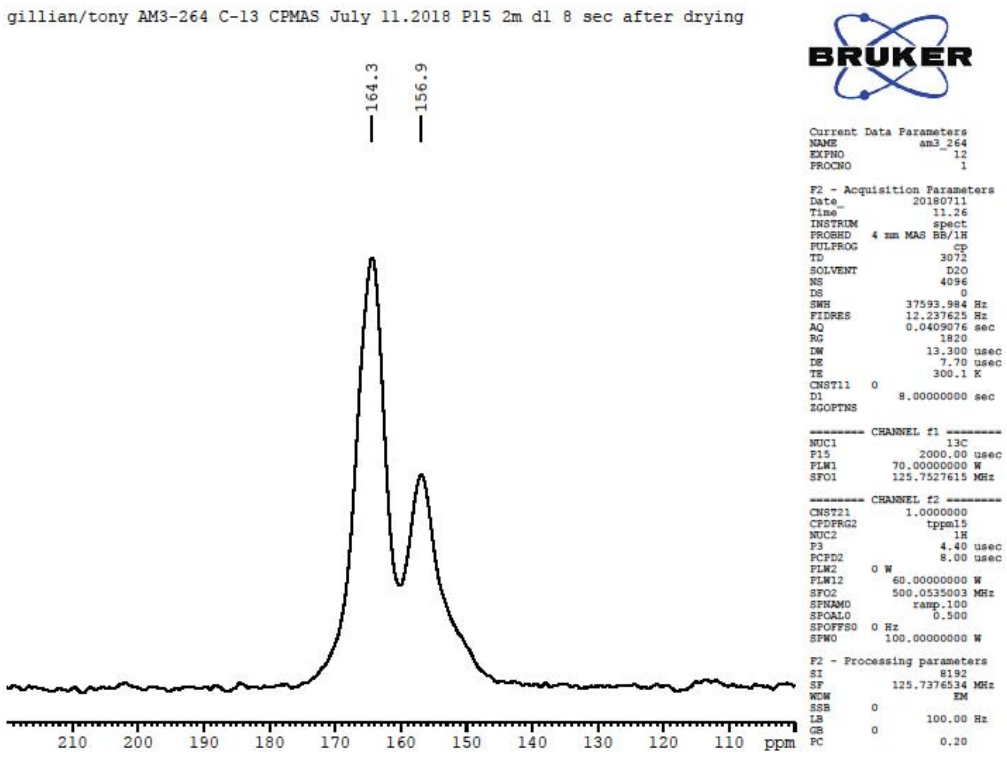


**Figure S3C**. CPMAS $^{13}C$ NMR of TCM-$C_3N_4$(T) sample.

**Table S1**. $^{13}C$ NMR shifts reported for carbon nitride materials.

| Sample | Shift of $C_{internal}$ (ppm) | Shift of $C_{external}$ (ppm) | ref |
|---|---|---|---|
| TCM-$C_3N_4$(P) | 156.6 | 164.3 | This work |
| TCM-$C_3N_4$(P/A) | 156.8 | 164.9 | This work |
| TCM-$C_3N_4$(T) | 156.9 | 164.3 | This work |
| $CN_xH_y$ (TCM 250 °C) | 156.6 | 164.6 | [1] |
| $CN_x$ (TAH 200 °C) | 156.0 | 163.7 | [2] |
| Phase 1 (MA 390 °C) | 155.3 | 166 | [3] |
| $CN_xH_y$ (MA 560-600 °C) | 157 | 164 | [4] |
| c-CN (DCDA 600 °C) | 157 | 165 | [5] |
| Urea-$CN_x$ (MA 550 °C) | 158.2 | 164.1 | [6] |

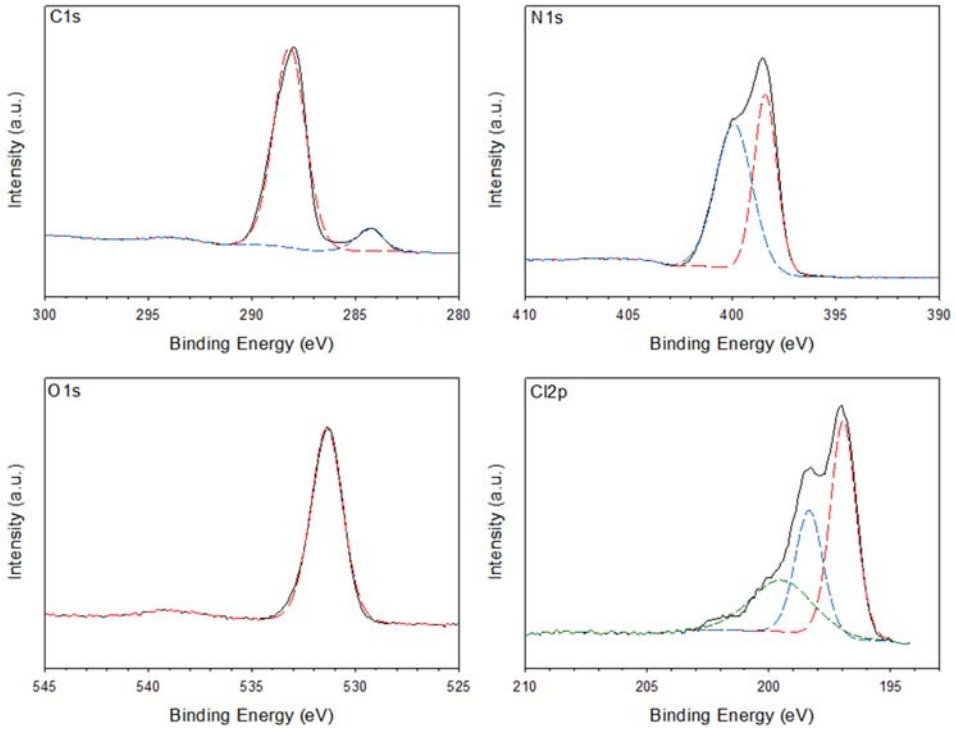


**Figure S4A**. Regional scan XPS data for TCM-$C_3N_4$(P) products on indium foil.

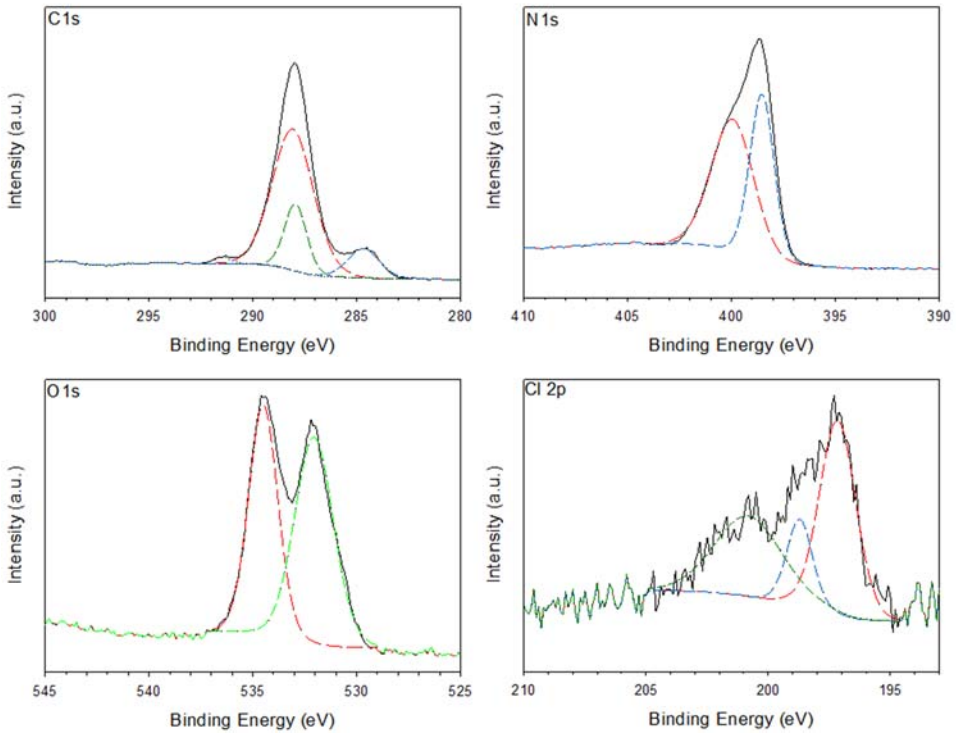


**Figure S4B**. Regional scan XPS data for TCM-$C_3N_4$(T) products on indium foil.

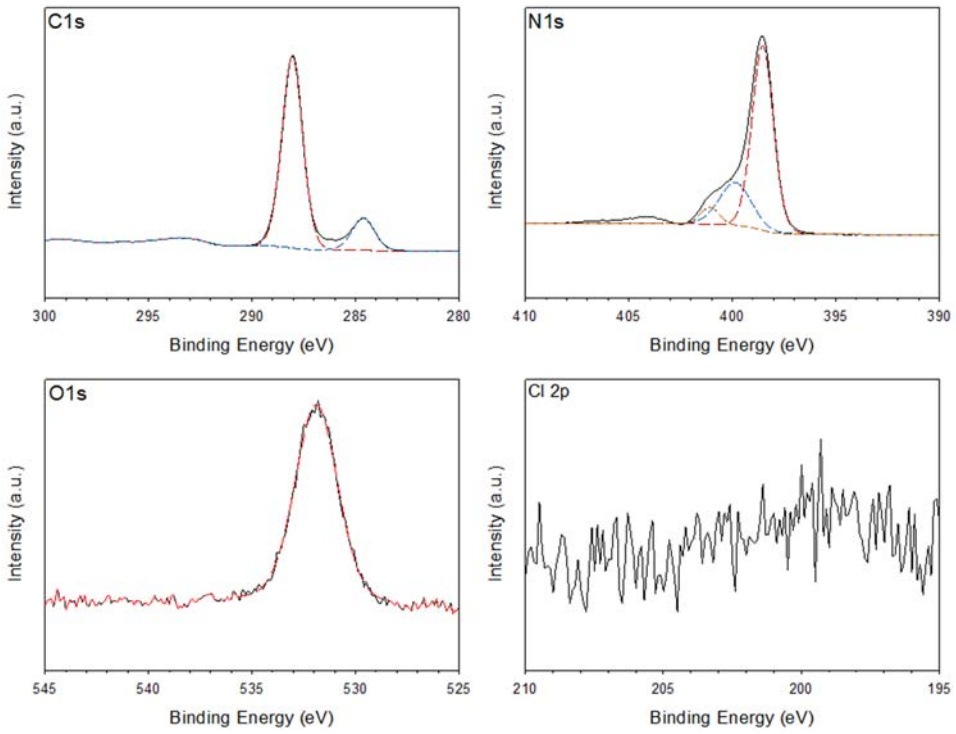


**Figure S4C**. Regional scan XPS data for TCM-$C_3N_4$(P/A) products on indium foil.

**Table S2**. XPS peak positions and compositional analysis for $C_3N_4$ products (major peak in **bold**). Compositions reported in parentheses omit contribution from adventitious carbon signal.

| Sample | C 1s (eV) | N 1s (eV) | O 1s (eV) | Cl 2p (eV) | Surface Composition |
|---|---|---|---|---|---|
| **TCM-$C_3N_4$(P)** | 284.34<br>**288.18** | **398.34**<br>399.92 | 531.38 | **196.94**<br>198.34<br>199.49 | $C_3N_{3.6}O_{0.8}Cl_{0.2}$<br>($C_3N_{4.0}O_{0.8}Cl_{0.1}$) |
| **TCM-$C_3N_4$(P/A)** | 284.62<br>286.22<br>**288.05** | **398.53**<br>399.86<br>401.1<br>404.5 | 531.88 | ND (not detected) | $C_3N_{3.4}O_{0.2}$<br>($C_3N_{4.2}O_{0.2}$) |
| **TCM-$C_3N_4$(T)** | 284.68<br>287.94<br>**288.07**<br>291.46 | **398.52**<br>399.94 | **532.05**<br>534.49 | **197.15**<br>198.71<br>200.83 | $C_3N_{2.6}O_{0.8}Cl_{0.05}$<br>($C_3N_{3.0}O_{1.0}Cl_{0.1}$) |

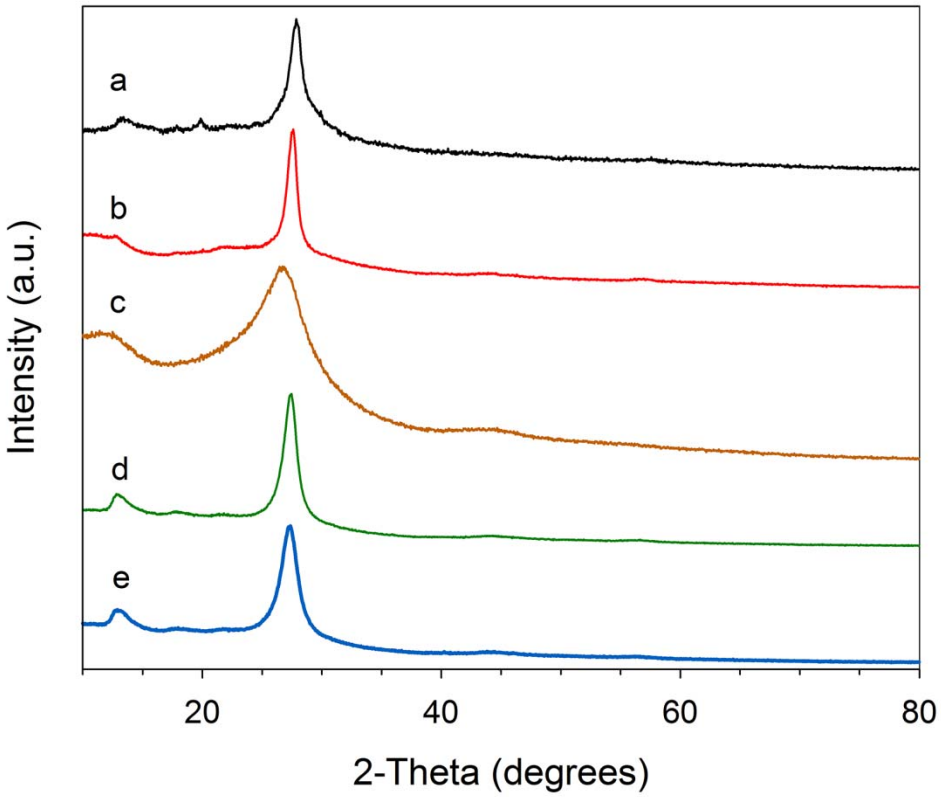


**Figure S5**. XRD patterns of (a) TCM-$C_3N_4$(P), (b) TCM-$C_3N_4$(P/A), (c) TCM-$C_3N_4$(T), (d) MA-$C_3N_4$(T), and (e) DCDA-$C_3N_4$(T).

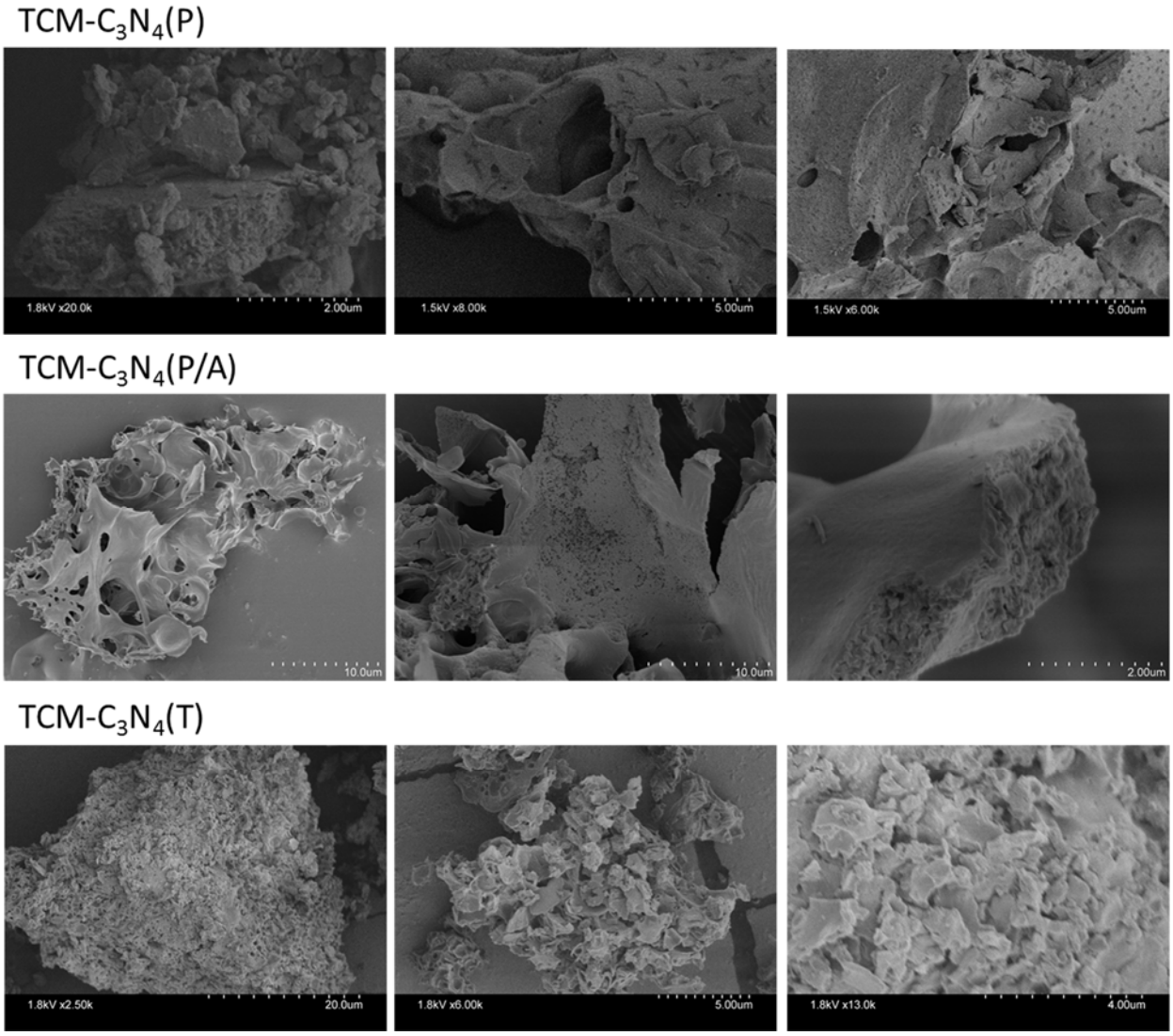


**Figure S6A**. Additional SEM images of (top row) TCM-$C_3N_4$(P), (middle row) TCM-$C_3N_4$(P/A), and (bottom row) TCM-$C_3N_4$(T).

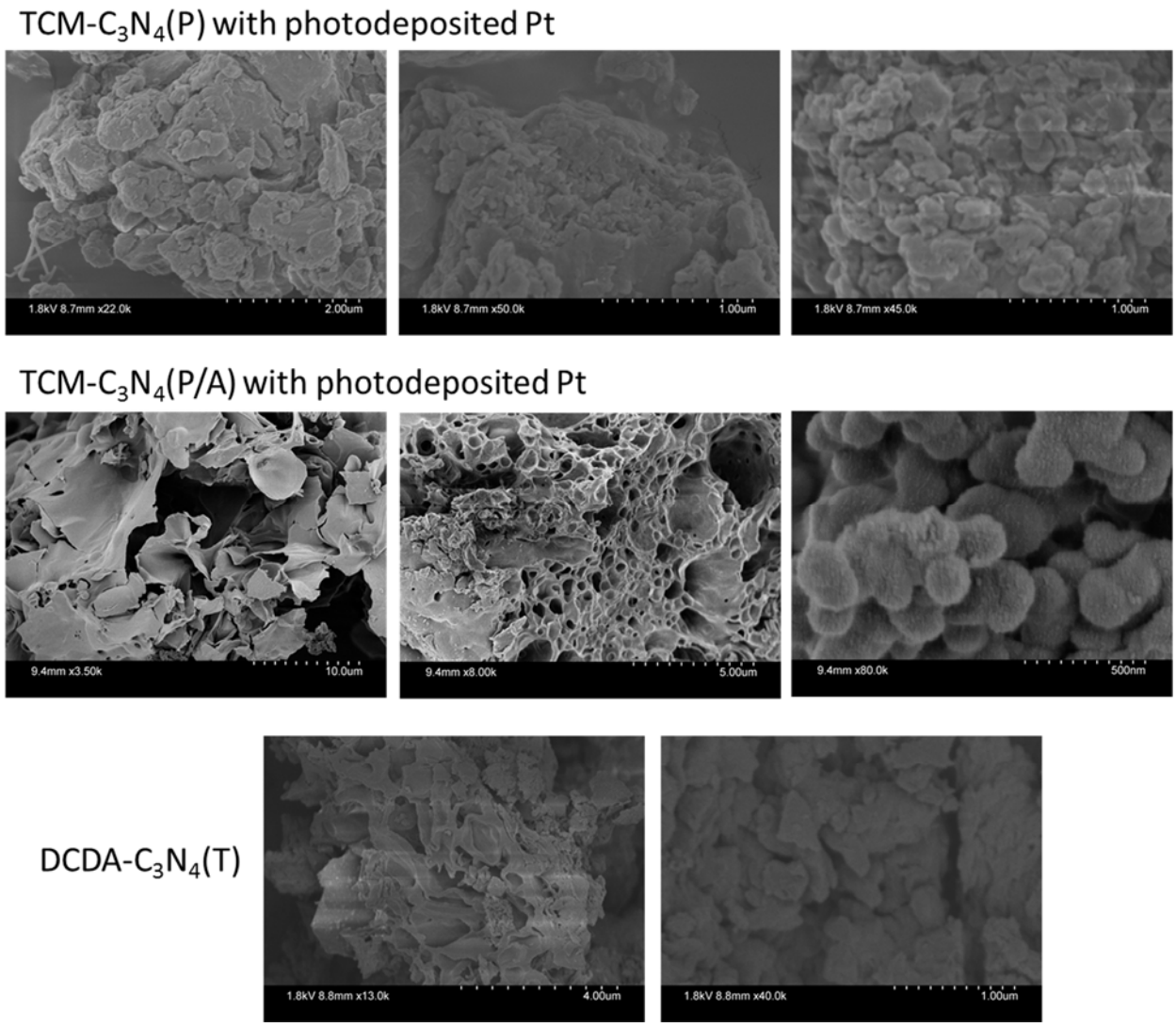


**Figure S6B**. Additional SEM images of (top row) TCM-$C_3N_4$(P) with deposited Pt, (middle row) TCM-$C_3N_4$(P/A) with deposited Pt, and (bottom row) DCDA-$C_3N_4$(T) product.

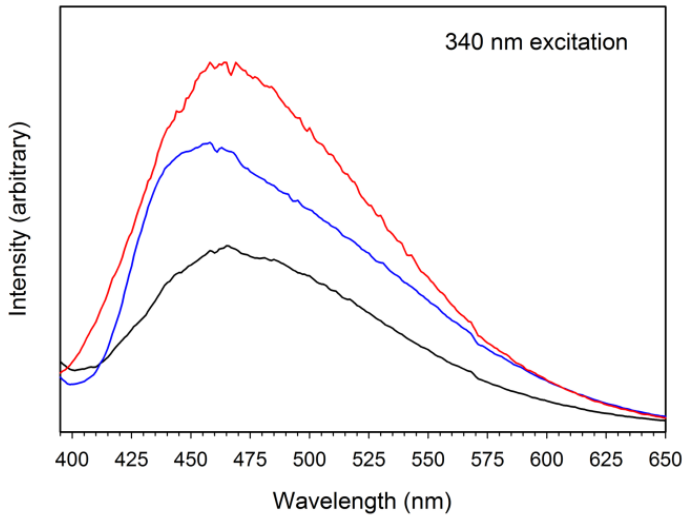


**Figure S7.** Comparison of solid-state room-temperature photoluminescence (PL) emission from TCM-$C_3N_4$(P) (red curve), TCM-$C_3N_4$(P/A) (blue curve), and TCM-$C_3N_4$(T) (black curve) taken at the same scan speed and detector sensitivity.

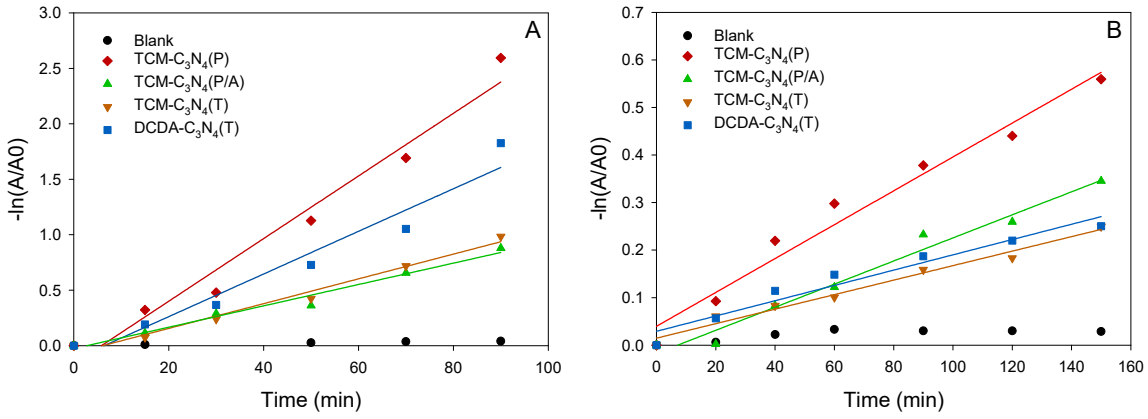


**Figure S8.** Linear rate fits for the degradation of methyl orange under (A) UV light and (B) visible light illumination.

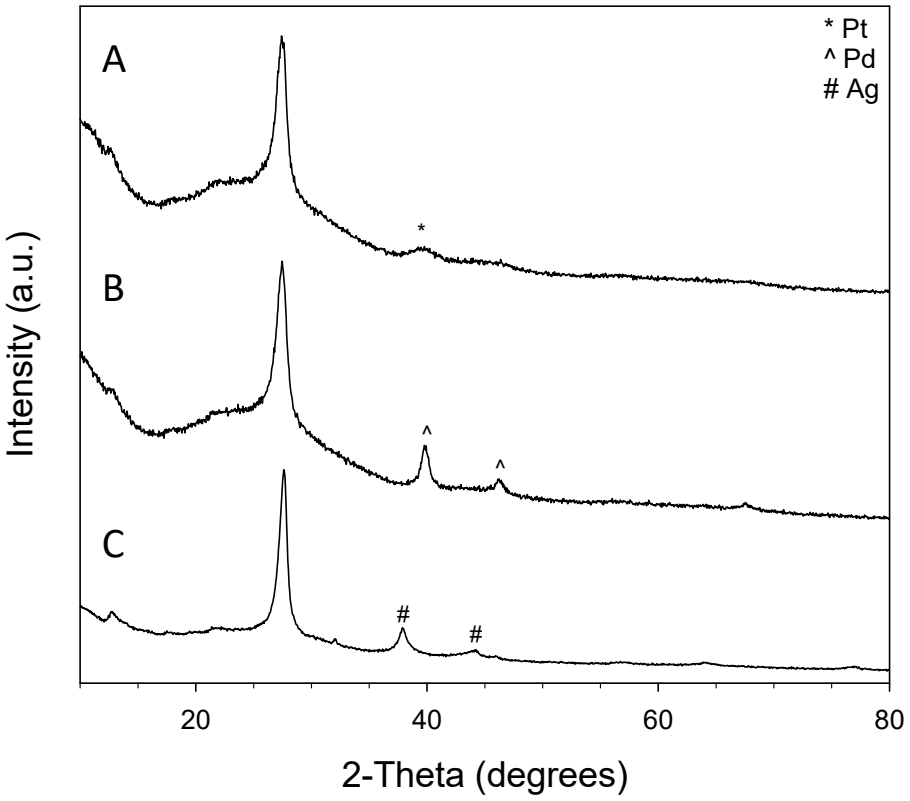


**Figure S9**. XRD of photodeposited cocatalyst metals (2-3 target wt%) on TCM-$C_3N_4$(P): (A) Pt, (B) Pd, and (C) Ag. Higher metal content used to identify elemental deposition.

**Table S3**. ICP-OES data for metal deposited on $C_3N_4$

| **Sample** | **Deposited Metal** | **Target M (w%)** | **Mass of M (mg)** | **Mass of Sample (mg)** | **Amount of M (wt%)** |
|---|---|---|---|---|---|
| TCM-$C_3N_4$(P) milled | Pt | 0.99 | 0.033 | 8.3 | 0.40 |
| TCM-$C_3N_4$(P/A) | Pt | 0.98 | 0.027 | 9.5 | 0.28 |
| TCM-$C_3N_4$(T) | Pt | 0.9 | 0.009 | 7.5 | 0.12 |
| TCM-$C_3N_4$(T) | Pt | 1.96 | 0.023 | 5.1 | 0.46 |
| MA-$C_3N_4$(T) | Pt | 0.98 | 0.032 | 11.5 | 0.28 |
| DCDA-$C_3N_4$(T) | Pt | 0.98 | 0.033 | 10.0 | 0.34 |
| TCM-$C_3N_4$(P) milled | Pd | 0.96 | 0.028 | 7.4 | 0.37 |
| TCM-$C_3N_4$(P) milled | Ag | 0.99 | 0.006 | 10.8 | 0.06 |

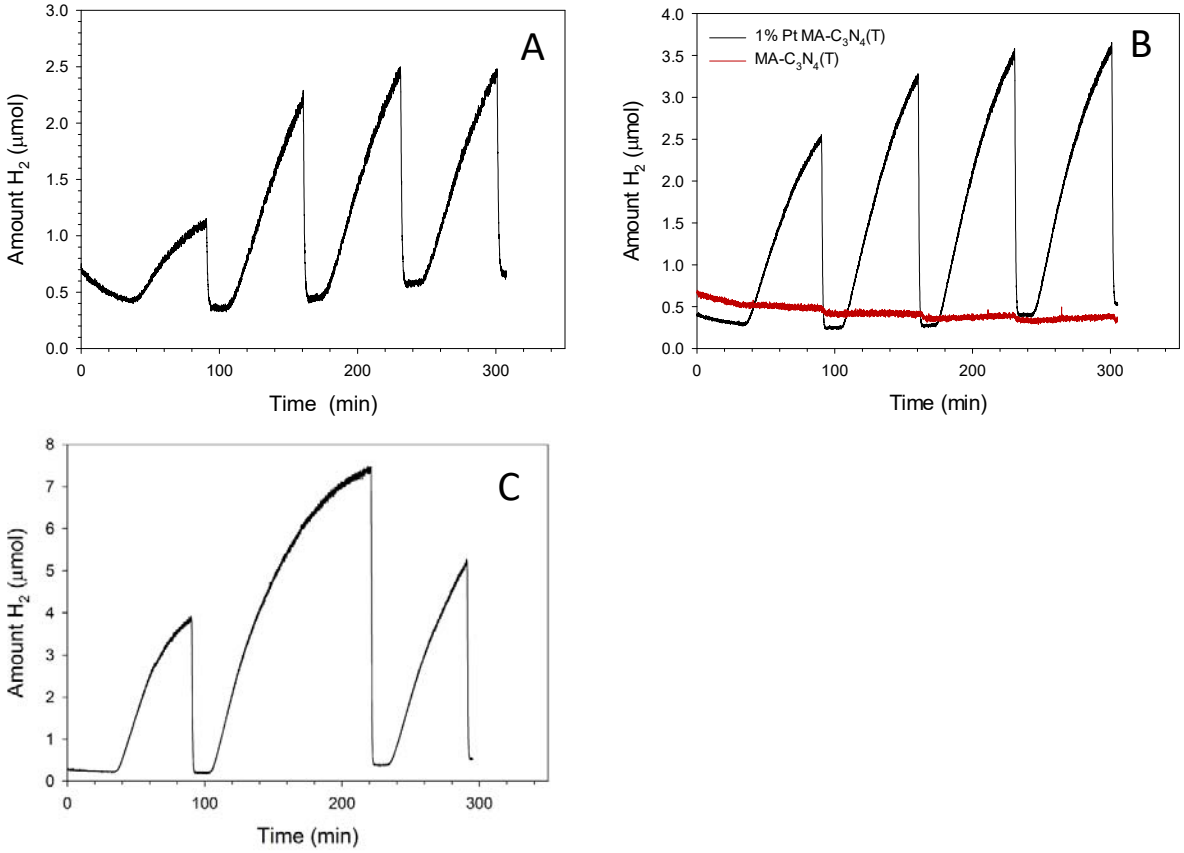


**Figure S10**. Hydrogen production cycles for carbon nitrides that used nominal 1% Pt coating solutions (A) TCM-$C_3N_4$(P/A) after coating it with a 1% Pt solution exhibiting delayed activation in the first cycle, (B) MA-$C_3N_4$(T) alone (red) and after coating it with a 1% Pt solution (black), and (C) DCDA-$C_3N_4$(T) after coating it with a 1% Pt solution – note double-time (2 hr) middle cycle showing $H_2$ evolution rate is maintained.

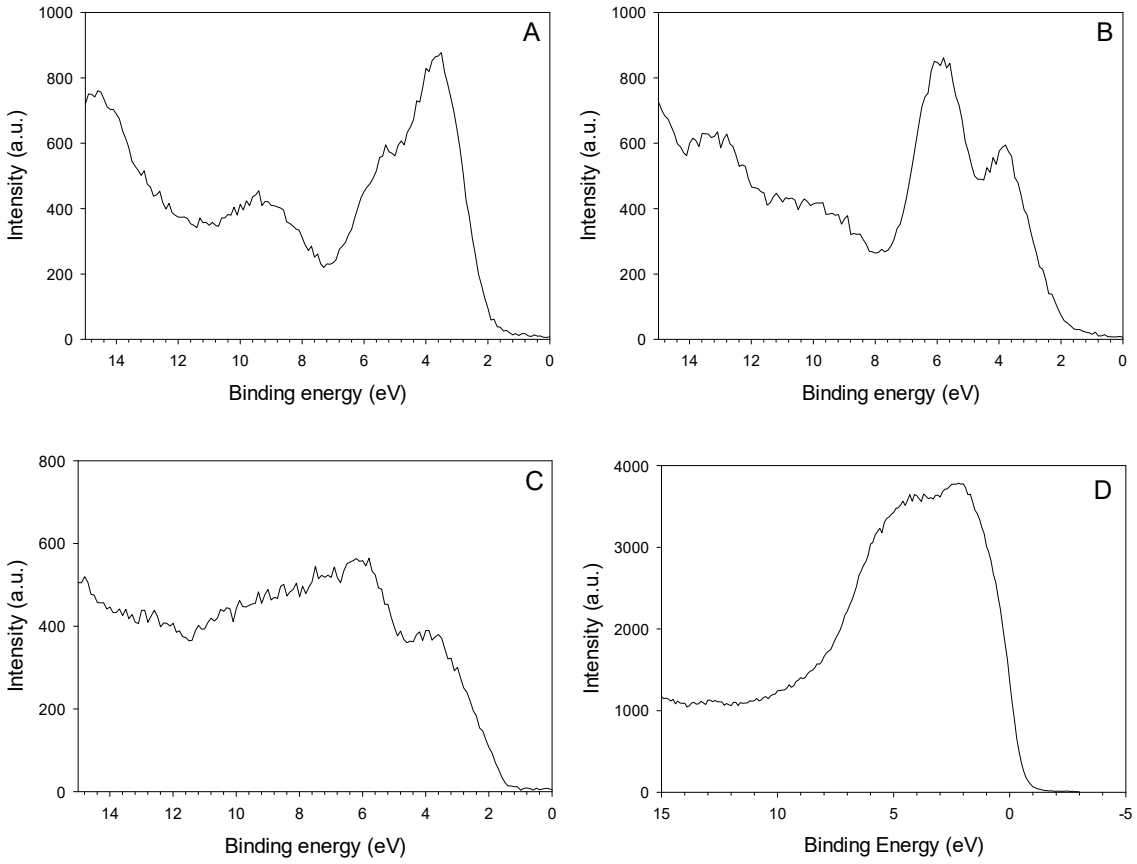


**Figure S11**. Valence band XPS spectra of (A) TCM-$C_3N_4$(P), (B) TCM-$C_3N_4$(P/A), (C) TCM-$C_3N_4$(T), and (D) Pt on TCM-$C_3N_4$(P/A).

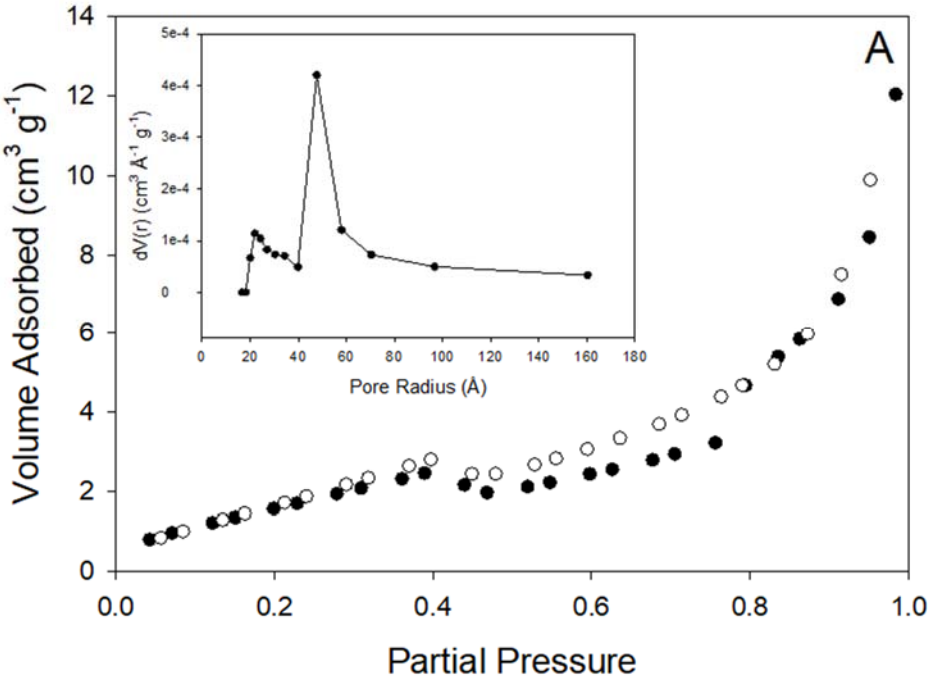
A
Volume Adsorbed (cm$^3$ g$^{-1}$)
Partial Pressure
dV(r) (cm$^3$ Å$^{-1}$ g$^{-1}$)
Pore Radius (Å)

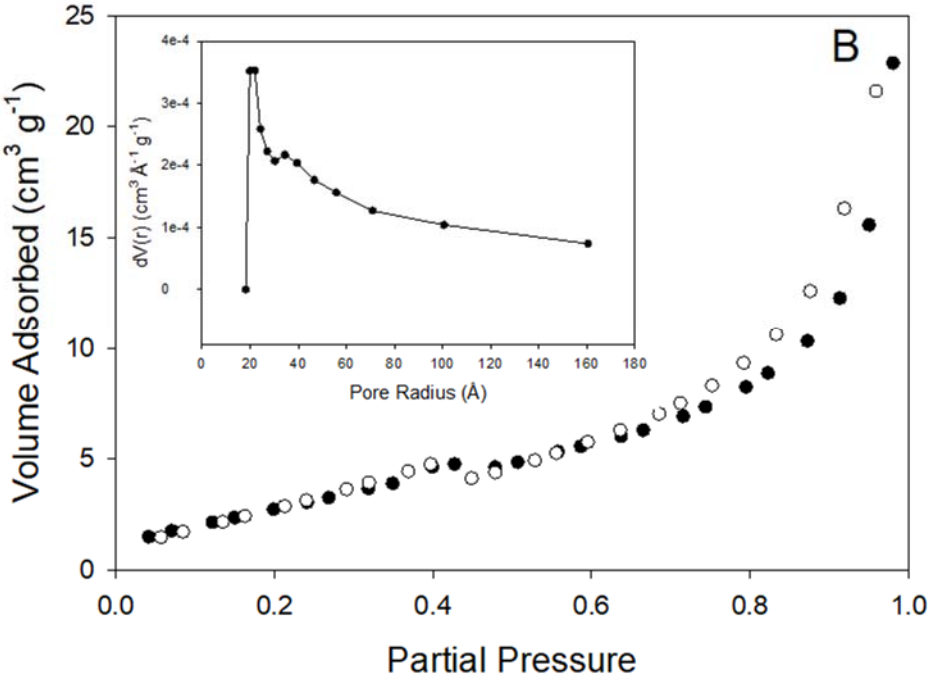
B
Volume Adsorbed (cm$^3$ g$^{-1}$)
Partial Pressure
dV(r) (cm$^3$ Å$^{-1}$ g$^{-1}$)
Pore Radius (Å)

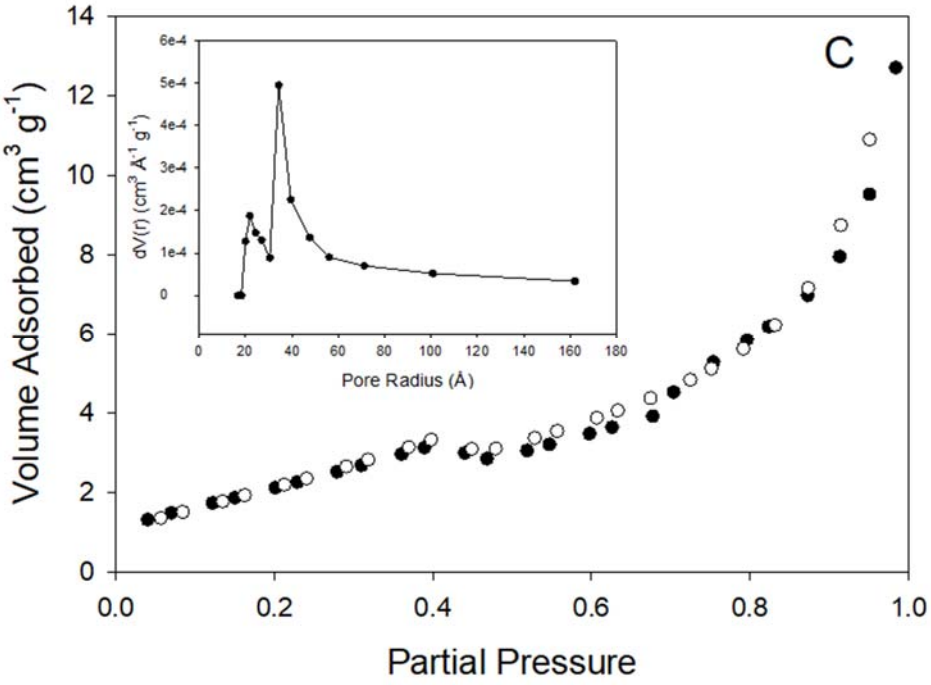


**Figure S12.** Nitrogen adsorption-desorption isotherms for (A) TCM-$C_3N_4$(P)-milled, (B) TCM-$C_3N_4$(P/A)-milled, and (C) TCM-$C_3N_4$(T)-milled. Black filled circles correspond to adsorption and open white circles are desorption data. Corresponding BJH pore size distributions are shown in the insets. Average pore radii are 47.7 Å, 21.9 Å, and 34.3 Å for TCM-$C_3N_4$(P)-milled, TCM-$C_3N_4$(P/A)-milled, and TCM-$C_3N_4$(T)-milled respectively.

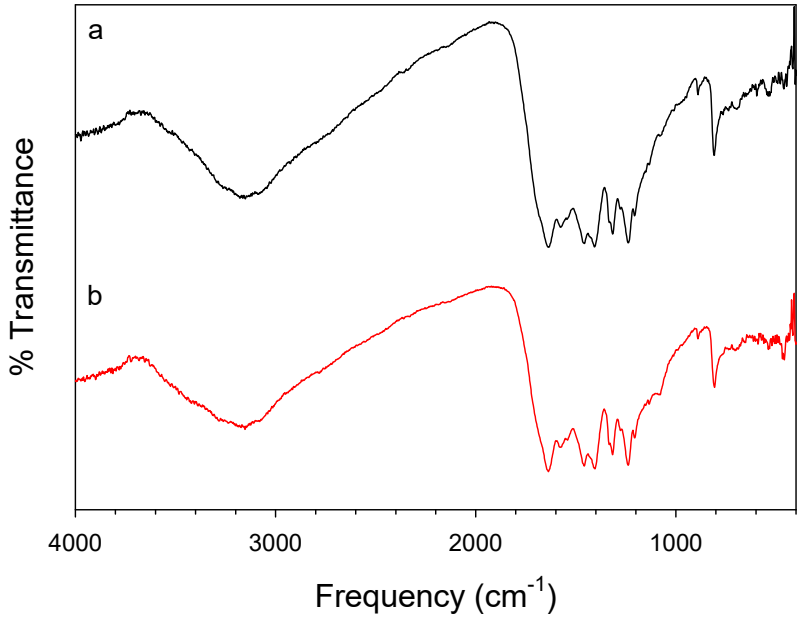


**Figure S13.** IR spectra of TCM-$C_3N_4$(P) (a) as synthesized and (b) after 4 hours of UV light exposure under oxygen atmosphere.

**Table S4.** Hydrogen evolution rates from selected comparable references.

| Catalyst | Conditions | $H_2$ Rate (μmol $h^{-1}$) | Ref. |
|---|---|---|---|
| 10 mg TCM-$C_3N_4$(P) – milled | 10% TEOA, 0.4% Pt, 450 W Hg lamp | 2.6 μmol $h^{-1}$ (260 μmol $h^{-1}$ $g^{-1}$) | This work |
| 10 mg TCM-$C_3N_4$(P/A) | 10% TEOA, 0.28% Pt, 450 W Hg lamp | 1.53 μmol $h^{-1}$ (153 μmol $h^{-1}$ $g^{-1}$) | This work |
| 10 mg TCM-$C_3N_4$(P/A) – milled | 10% TEOA, 0.49% Pt, 450 W Hg lamp | 1.93 μmol $h^{-1}$ (193 μmol $h^{-1}$ $g^{-1}$) | This work |
| 100 mg $C_3N_4$ (DCDA 550 °C) | 10% TEOA, 6% Pt, 300 W Xe lamp (>300 nm) | 20 μmol $h^{-1}$ (200 μmol $h^{-1}$ $g^{-1}$) | 7 |
| 50 mg bulk g-$C_3N_4$ (DCDA 550 °C) | 10% TEOA, 6% Pt, 300 W Xe lamp (UV) | 31.5 μmol $h^{-1}$ (630 μmol $h^{-1}$ $g^{-1}$) | 8 |
| gCNM (MA/DCDA 550 °C) | 10% MeOH, 75 W Xe lamp (UV) | 1.5 μmol $h^{-1}$ | 9 |
| 100 mg Bulk CN (DCDA) | 10% TEOA, 1% Pt, 300 W Xe lamp (>420 nm) | 1.2 μmol $h^{-1}$ (12 μmol $h^{-1}$ $g^{-1}$) | 5 |
| 20 mg Bulk $C_3N_4$ (MA 550 °C) | 10% TEOA, 300 W Xe lamp (>420 nm) | 6.1 μmol $h^{-1}$ $g^{-1}$ | 10 |
| 20 mg Bulk $C_3N_4$ (MA 550 °C) | 10% TEOA, 3% Pt, 300 W Xe lamp (>420 nm) | ~ 400 μmol $h^{-1}$ $g^{-1}$ | 10 |
| 0.1 g CN (DCDA 550 °C) | 10% TEOA, 3% Pt, 300 W Xe lamp (>400nm) | 3.9 μmol $h^{-1}$ (39 μmol $h^{-1}$ $g^{-1}$) | 11 |
| 0.1 g g-$C_3N_4$ (cyanamide 550 °C) | 10% TEOA, 3% Pt, 500 W Hg lamp (>420 nm) | 18 μmol $h^{-1}$ (180 μmol $h^{-1}$ $g^{-1}$) | 12 |
| 0.1 g mpg-$C_3N_4$ (cyanamide550 °C) | 10% TEOA, 3% Pt, 500 W Hg lamp (>375 nm) | 300 μmol $h^{-1}$ (180 μmol $h^{-1}$ $g^{-1}$) | 12 |


1. Holst, J. R.; Gillan, E. G. From triazines to heptazines: Deciphering the local structure of amorphous nitrogen-rich carbon nitride materials. *J. Am. Chem. Soc.* **2008,** *130* (23), 7373-9.

2. Miller, D. R.; Holst, J. R.; Gillan, E. G. Nitrogen-rich carbon nitride network materials via the thermal decomposition of 2,5,8-triazido-s-heptazine. *Inorganic chemistry* **2007,** *46* (7), 2767-74.

3. Lotsch, B. V.; Schnick, W. New light on an old story: Formation of melam during thermal condensation of melamine. *Chemistry* **2007,** *13* (17), 4956-68.

4. Lotsch, B. V.; Doblinger, M.; Sehnert, J.; Seyfarth, L.; Senker, J.; Oeckler, O.; Schnick, W. Unmasking melon by a complementary approach employing electron diffraction, solid-state NMR spectroscopy, and theoretical calculations-structural characterization of a carbon nitride polymer. *Chemistry* **2007,** *13* (17), 4969-80.

5. Rahman, M. Z.; Tapping, P. C.; Kee, T. W.; Smernik, R.; Spooner, N.; Moffatt, J.; Tang, Y.; Davey, K.; Qiao, S.-Z. A benchmark quantum yield for water photoreduction on amorphous carbon nitride. *Adv. Funct. Mater.* **2017,** *27* (39), 1702384.

6. Lau, V. W.-h.; Yu, V. W.-z.; Ehrat, F.; Botari, T.; Moudrakovski, I.; Simon, T.; Duppel, V.; Medina, E.; Stolarczyk, J. K.; Feldmann, J.; Blum, V.; Lotsch, B. V. Urea-modified carbon nitrides: Enhancing photocatalytic hydrogen evolution by rational defect engineering. *Advanced Energy Materials* **2017,** *7* (12), 1602251.

7. Liu, G.; Niu, P.; Sun, C.; Smith, S. C.; Chen, Z.; Lu, G. Q.; Cheng, H. M. Unique electronic structure induced high photoreactivity of sulfur-doped graphitic C3N4. *J. Am. Chem. Soc.* **2010,** *132* (33), 11642-8.

8. Niu, P.; Zhang, L.; Liu, G.; Cheng, H.-M. Graphene-like carbon nitride nanosheets for improved photocatalytic activities. *Adv. Funct. Mater.* **2012,** *22* (22), 4763-4770.

9. Jorge, A. B.; Martin, D. J.; Dhanoa, M. T. S.; Rahman, A. S.; Makwana, N.; Tang, J.; Sella, A.; Corà, F.; Firth, S.; Darr, J. A.; McMillan, P. F. H2 and o2 evolution from water half-splitting reactions by graphitic carbon nitride materials. *J. Phys. Chem. C* **2013,** *117* (14), 7178-7185.

10. Chen, Z.; Fan, T.-T.; Yu, X.; Wu, Q.-L.; Zhu, Q.-H.; Zhang, L.-Z.; Li, J.-H.; Fang, W.-P.; Yi, X.-D. Gradual carbon doping of graphitic carbon nitride towards metal-free visible light photocatalytic hydrogen evolution. *Journal of Materials Chemistry A* **2018,** *6* (31), 15310-15319.

11. Xing, W.; Tu, W.; Han, Z.; Hu, Y.; Meng, Q.; Chen, G. Template-induced high-crystalline g-C3N4 nanosheets for enhanced photocatalytic h2 evolution. *ACS Energy Letters* **2018,** *3* (3), 514-519.

12. Wang, X.; Maeda, K.; Chen, X.; Takanabe, K.; Domen, K.; Hou, Y.; Fu, X.; Antonietti, M. Polymer semiconductors for artificial photosynthesis: Hydrogen evolution by mesoporous graphitic carbon nitride with visible light. *J. Am. Chem. Soc.* **2009,** *131* (5), 1680-1.